Knox, G.W., McInnes, C.R., Younger, P.L. and Sloan, W.T. (2019) Engineering artificial thermal mountains for large-scale water management and carbon drawdown. *Environmental Science: Water Research and Technology*, 5(2), pp. 296-314. (doi:10.1039/c8ew00571k)

Engineering Artificial Thermal Mountains for Large-Scale Water Management and Carbon Drawdown

Knox, G. W. McInnes, C. R. Younger, P. L. and Sloan, W.T.
School of Engineering, University of Glasgow, Glasgow G12 8QQ, UK’

Abstract

To meet future climate change targets, it may become necessary to remove carbon dioxide from the atmosphere at an unprecedented rate and scale. This paper investigates a new potential strategy: the application of the thermal mountain effect to artificially increase rainfall in desert regions and transform such regions into a vegetated state, thus sequestering significant quantities of carbon. A preliminary systems engineering analysis evaluating the design parameters of an artificial thermal mountain is provided, along with the analysis of its potential for carbon capture and agricultural applications. It is estimated that a large-scale low-albedo coating, between 15,000 and 50,000 km^2 in surface area, would, in principle, be sufficient to provide enough rainfall to irrigate a 1000 km x 2000 km section of the Sahara desert. While the scale of engineering is potentially vast, it is arguably smaller than other schemes such as enhanced rock weathering.

ACKNOWLEDGEMENTS

The kind support of the Henry Baxter Scholarship (GK) and a Royal Society Wolfson Research Merit Award (CM) is gratefully acknowledged.

1 INTRODUCTION

While pursuing conventional emission reduction strategies is key to climate change mitigation, the uncertainty of the growth and impact of increasing CO$_2$ concentration[1] means that it is also important to consider more extreme carbon negative strategies. This is particularly relevant in the wake of the COP21 climate change agreement, whose future emission reduction targets rely upon a range of speculative carbon-negative technologies.[2] The preliminary investigation of such technologies is, therefore, an imperative, both to fully explore the range of possible technologies and to assess their potential.

A speculative, but potentially scalable solution, for large-scale carbon drawdown is the afforestation of desert regions through the use of artificial thermal mountains. For example, the Sahara desert has been vegetated many times; indeed, a Saharan rainforest was recent enough to coexist with early human cultures.[3] Brovkin et al suggests that this region exists in a quasi-stable state; small changes in solar insolation driven by the Earth's orbital eccentricity and axial tilt caused it to shift from a vegetated state to its current arid state.[4] However, in the same vein, engineering intervention could potentially reverse this transition, a process that is in fact aided by increasing atmospheric CO_2. Should this be achieved, the resultant carbon sink could, in principle, reverse the entirety of human CO_2 emissions since the industrial revolution, presenting an intriguing opportunity for large-scale mitigation.[5] However, a recent study using numerical climate models has indicated that these feedback effects may not be as significant as Brovkin et al suggests, and much of the evapotranspirated water moves further South rather than falling as precipitation on the Sahara.[6]

Previous studies of achieving a green Sahara through direct irrigation estimate that to supply the region with enough desalinated water would require the equivalent of approximately 4500 nuclear power plants.[5] However, the thermal mountain effect may present a more effective, although still challenging, strategy. The thermal mountain effect is a naturally occurring phenomenon whereby large temperature differences at ground level, such as a forest fire, can force air upwards, where it cools, and thereby induces precipitation.[7] This phenomenon has been induced unintentionally; in Australia, a long wildlife-proof fence separates large areas of native vegetation from agricultural land. The formation of clouds along the lower-albedo native vegetation is enhanced compared to the lighter agricultural land.[8] The same effect could, in principle, be created artificially by engineering the landscape to create a localised area of high temperature contrast. The concept was first proposed in the 1960s in the form of long asphalt strips in the desert —-

low-albedo asphalt would absorb more solar radiation than the surrounding sand, and provide the temperature difference necessary to create a thermal mountain.[7] Figure 1 shows a schematic of this concept.

However, the concept received criticism when first proposed.[9] It was claimed that initial studies overestimated the potential for precipitation caused by the thermal mountain, and the method of comparing thermal mountain profiles to physical mountain profiles and extrapolating precipitation levels from environmental data ignored a large range of external factors. In addition, using vast quantities of asphalt may also be undesirable for environmental reasons.

The use of thermal mountains to create carbon sinks has a number of advantages over other climate change mitigation strategies. Unlike carbon capture and storage, it actively removes carbon from the air, rather than lowering the emission of carbon from fossil fuel power plants. Solar radiation management can be used to reduce increasing temperatures caused by growing CO_2 concentration, but must be actively maintained.[10] The use of enhanced rock weathering is another potential mitigation strategy, through the distribution of pulverised rock throughout the tropics and allowing rock weathering to provide passive carbon drawdown. However, both the land area and mass of material necessary for intervention are potentially orders of magnitude above that estimated here for artificial thermal mountains.[11]

A recent study by Li et al[12] investigated the use of large-scale solar and wind farms in the Sahara, and their impact on the local climate. Using a climate model

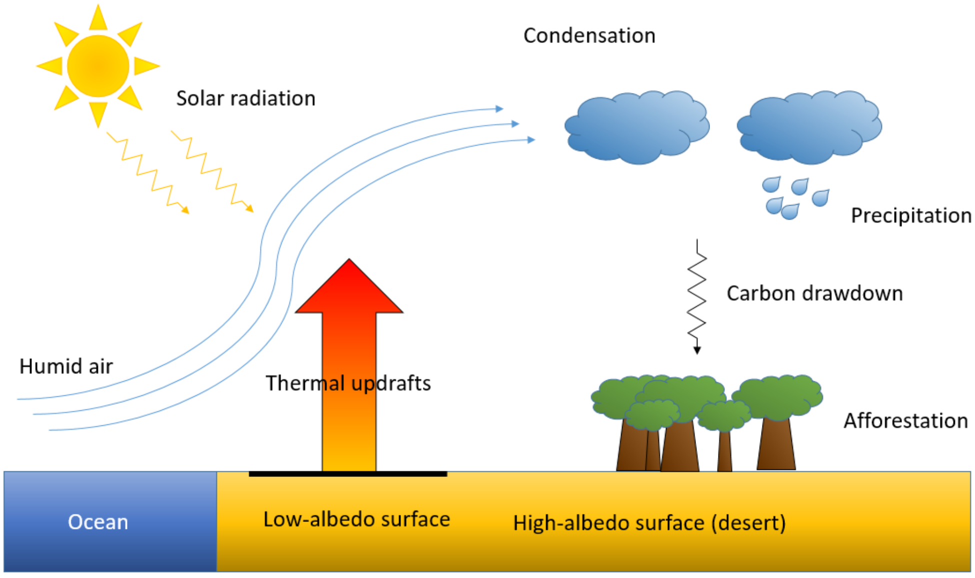

Fig. 1: Conceptual schematic of the thermal mountain effect.

coupled with dynamic vegetation, solar and wind farms were modelled by altering surface friction and albedo accordingly, and it was found that precipitation was increased by 150%, with some areas increasing by as much as 500 mm yr^{-1}.

This paper seeks to develop a preliminary, systems engineering strategy for calculating the potential for precipitation induced by an artificial thermal mountain, and from this investigate the basic parameters relating to sizing the thermal mountain. The precipitation potential is coupled with a simple model of vegetation-precipitation feedback and from this establishes the scale of thermal mountain system necessary to achieve a vegetated Sahara. An approximate model of a thermal mountain system is presented, driven by numerical climate model data (CFS dataset), covering the precipitation targets, key thermodynamic processes and estimating the precipitation induced. This provides an order-of-magnitude estimate as to the scale of intervention required to achieve a vegetated Sahara. Agricultural applications and analysis of water transport are also presented, alongside optimisation of the concept to provide increased efficiency, or reduced scale of intervention. Clearly, the analysis presented is approximate, to provide order of magnitude estimates of precipitation for engineering analysis. Future work will investigate the use of more complex numerical tools and climate models.

The paper is organised as follows: in Section 2, the effects of precipitation-vegetation interaction are discussed, and precipitation targets defined. In Section 3, the thermal mountain model is presented, covering the climate data used to drive the model, the key thermodynamic processes and precipitation estimation. In Section 4, key results used in calculating the scale of thermal mountain required are presented. In Section 5, the accuracy of the model and sources of error are discussed. Section 6 discusses the potential for carbon drawdown using tree plantations in conjunction with thermal mountains. Section 7 provides an analysis of agricultural applications and water supply requirements. The discussion in Section 8 covers a range of variations of the thermal mountain concept.

2 VEGETATION-PRECIPITATION INTERACTION

Using a conceptual model describing the interaction of climate and desert vegetation[4] it is possible to establish basic design goals for a thermal mountain system. The model represents vegetation as a function of precipitation, and vice versa, the former of which is justifiable as precipitation is the primary driver of vegetation growth in such a dry climate. Precipitation is also a function of vegetation due to the change in surface albedo and roughness that vegetation causes and its subsequent impact on the local climate. Other positive feedbacks can be of importance, such as establishing trees whose deep roots can access underground aquifers, allowing smaller plants access to this water through evapotranspiration, or larger plants providing the necessary shade for smaller plants to flourish.[13] Of key importance in the model is the existence of multiple stable equilibria, suggesting that through engineering intervention the system could be forced from one equilibrium to another, after which the system would sustain itself at the new equilibrium state. This is relevant to the artificial thermal mountain problem as it can set a minimum target for the precipitation delivered by a thermal mountain system. The minimum target is the additional baseline precipitation necessary for the system to have a single, wet, vegetated equilibrium state.

The conceptual non-linear vegetation-precipitation model is described by Eq. 1, based on the analysis of Brovkin et al,[4] where V ($0 \leq V \leq 1$) is the fractional vegetation coverage and P the precipitation (mm yr^{-1}), while V^* and P^* are the equilibrium states of these variables. P_{cr} is the minimum precipitation level for vegetation growth, P_d the existing baseline precipitation and a and b are system parameters. Calibrated by data from a climate model simulating a 1000 km North-South, 2000 km West-East box covering a section of the Sahara desert,[4] the fixed parameters are $P_{cr} = 120$ mm yr^{-1}, $P_d = 40\,\mathrm{mm}$ yr^{-1}, $a = 5 \times 10^{-5}$ and $b = 590$, such that:

$$V^*(P) = \begin{cases} 0 & P < P_{cr} \\ 1 - \frac{1}{(1+a(P-P_{cr})^2} & P \geq P_{cr} \end{cases} \tag{1a}$$

$$P^*(V) = P_d + bV \tag{1b}$$

By substituting Eq. 1b into Eq. 1a, the following cubic function is found:

$$\begin{gathered} ab^2V^3 + (2ab(P_d - P_{cr}) - ab^2)V^2 \\ +(1 + a(P_d - P_{cr})^2 - 2ab(P_d - P_{cr}))V \\ -a(P_d - P_{cr})^2 = 0 \end{gathered} \tag{2}$$

The discriminant Δ of Eq. 2 can then be calculated using the general solution for a cubic equation, such that:

$$\Delta = 18ABCD - 4B^3D + B^2C^2$$
$$-4AC^3 - 27A^2D^2 \tag{3a}$$

where the coefficients

$$A = ab^2 \tag{3b}$$

$$B = (2ab(P_d - P_{cr}) - ab^2) \tag{3c}$$

$$C = (1 + a(P_d - P_{cr})^2 - 2ab(P_d - P_{cr})) \tag{3d}$$

$$D = -a(P_d - P_{cr})^2 \tag{3e}$$

are related to the model parameters. When $\Delta < 0$, there exists only a single real root. The values of P_d which satisfy this condition are $39.75\,\mathrm{mm}$ yr^{-1} and $142\,\mathrm{mm}$ yr^{-1}, therefore for values of $P_d < 39.75\,\mathrm{mm}$yr^{-1}, there exists only a single, dry equilibrium state, and likewise, for values of $P_d > 142\,\mathrm{mm}$ yr^{-1}, there exists only a single, wet equilibrium state. Figure 2 shows the results of the conceptual model. The solid line shows equilibrium vegetation coverage as a function of precipitation (Eq. 1a), while the straight lines show equilibrium precipitation as a function of vegetation coverage (Eq. 1b); P_1(V) shows present day conditions, whilst P_2(V) shows the maximum baseline precipitation which still exhibits multiple equilibria; beyond P_2(V) there exists a single, vegetated equilibrium point. The points where the lines intersect are then the stable equilibria for the coupled system. If the baseline precipitation was increased to a position beyond the dotted line ($P_d > 142\,\mathrm{mm}$ yr^{-1}, from the present 40 mm yr^{-1}) then the system would bifurcate to its stable vegetated state. Note that the timescale in reaching this equilibrium state is not considered, although the relaxation timescale for vegetation can range from years to decades.[4]

This conceptual model, therefore, provides an approximate engineering requirement for a thermal mountain system with sufficient output to increase precipitation across the 1000 km × 2000 km desert box by approximately 100 mm yr^{-1}. This would, in principle, be sufficient to shift the system into a single, vegetated equilibrium state, which it would then relax to, over a timescale of order decades. If this additional precipitation were subsequently removed, the system would relax

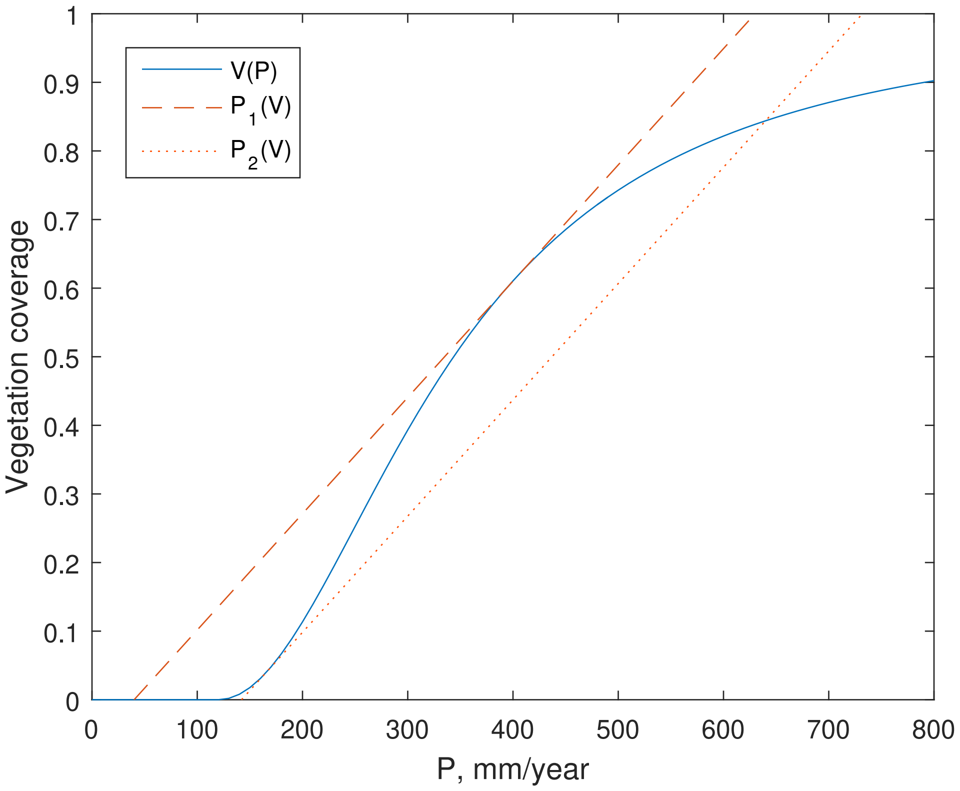

Fig. 2: Vegetation-precipitation model showing V(P), current precipitation (P_1) and maximum precipitation for multiple equilibria (P_2)

back to the equilibrium at $V \sim 0.6$, rather than the to dry equilibrium, at $V \sim 0$.

3 MODELLING THE THERMAL MOUNTAIN EFFECT

The model of the thermal mountain system consists of three parts: a thermodynamic model describing the hourly temperature profile of the surface of the sand and low-albedo coating, a model describing the effects on air flowing over the engineered surface, and a precipitation model. Each successive model is driven by the results of the previous one to deliver a precipitation estimate for the entire thermal mountain system. The model is partly driven by data from a numerical climate model (CFS dataset), although it is not directly coupled to it. Although approximate, the model is sufficient to provide engineering estimates of enhanced precipitation required to size the thermal mountain system. Figure 3 provides a schematic of the key features of the thermal mountain model.

For the sake of clarity when describing the geometry, length (denoted as L in equations and diagrams) will always describe the distance a thermal mountain system extends from the edge of the $1000\,\text{km} \times 2000\,\text{km}$ box in towards the centre, the direction denoted in Figure 3 as x. Breadth will always describe the distance along the edge of the box, the direction denoted in Figure 3 as y.

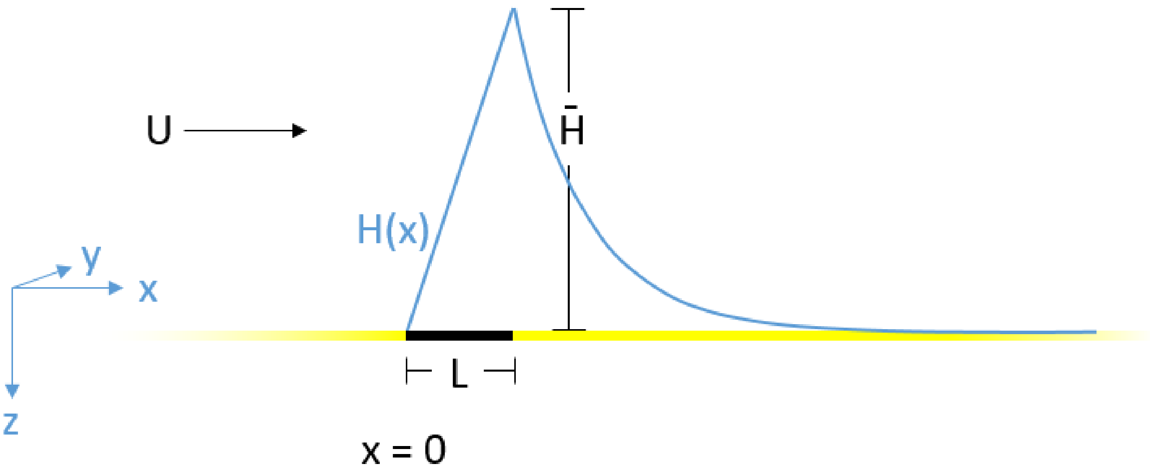

Fig. 3: Schematic of the thermal mountain effect, describing geometry of a low-albedo surface of length L, equivalent height profile of $H(x)$ and wind speed U.

Figure 4 shows the flow of data between the sub-models. Soil temperature, air temperature, wind speed and humidity are all inputs used to drive the top-level model.

The model is intended as a low-order engineering approximation, therefore several assumptions have been made. Within the thermodynamic model, it is assumed that the convective heat transfer coefficient can be taken as constant, and that beyond lowered albedo, the engineering intervention has no other impact on the thermodynamics of the system. Therefore, both sand and asphalt can be treated equally with the same model. Within the airflow model, the mixing length and environmental lapse rate are unknown, and are assigned reasonable approximate values. It is also assumed that across timestep iterations, the system rapidly reaches steady state and its properties can be taken as constant for the duration of that timestep. Through the use of the CFS data as input, there is also the assumption that the engineering intervention will not significantly affect these parameters, which may not necessarily be the case. These assumptions are discussed more closely within the subsections for each model.

MATLAB was used for all numerical processes throughout. Most of the numerics were standard, however, notably, Equation 4 was resolved using a basic implementation of the Thomas algorithm.

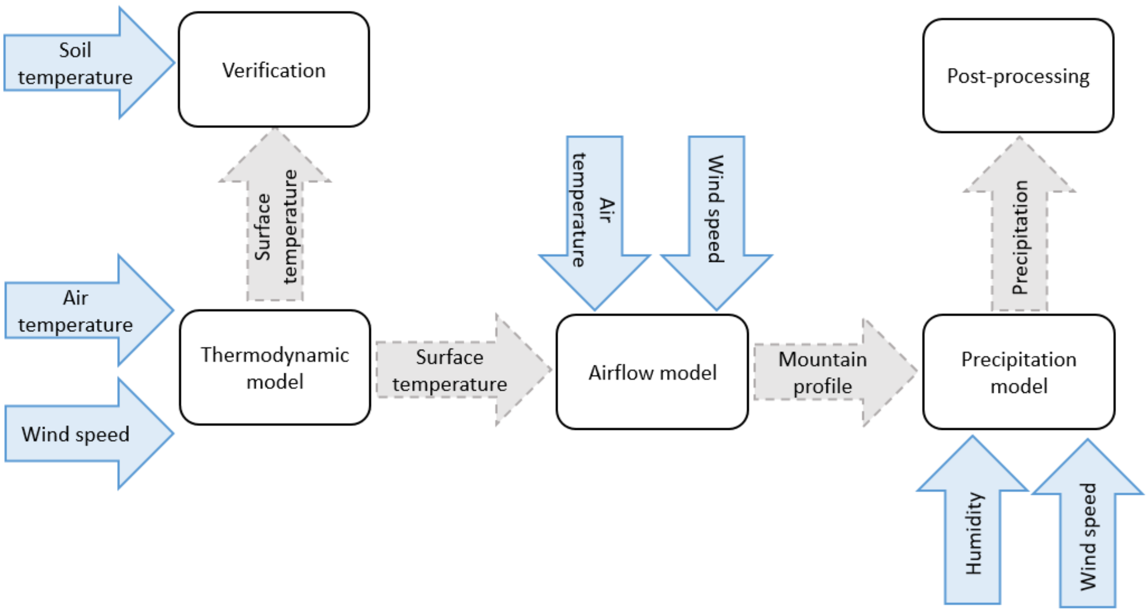

Fig. 4: Flowchart describing flow of data between sub-models.

3.1 Climate Data

In order to provide a more realistic analysis of the thermal mountain effect, the model is driven by data from the National Center for Environmental Prediction's Climate Forecast System v2 Operational Analysis Time Series (henceforth referred to as CFS). This database was used to provide wind speed, air temperature and humidity data in order to drive the model, and ground temperature at a depth of 5 cm in order to verify the accuracy of the thermodynamic model.[14] The database provides high resolution datasets (hourly data points, approximately 38 km spatial separation) for various environmental parameters.[15] Across the 1000 km × 2000 km desert box, there are 51 latitudinal points and 138 longitudinal points. Datasets exist covering 1979 to 2016, however, due to computational constraints only 2015 was considered. It is possible that computation over a longer period would reveal some annual variations to the thermal mountain effect. Note that while CFS is intended to provide a good estimate of the environmental parameters, their accuracy is less important to this study than the fact that they are a set of values which capture seasonal variation, and that the temperature, wind speed and humidity are realistic with respect to each other at any particular timestep. Clearly, the presence of large-scale low-albedo surfaces would have a significant impact upon local environmental parameters in the vicinity of the thermal mountain, which is not captured here. However, the data sets provide the flux of moisture across the thermal mountain region for engineering analysis, which can be used as inputs and boundary conditions to drive the model.

3.2 Thermodynamic Modelling

The thermodynamic model is a simple one-dimensional model, an extension of the classical heat equation (Eq. 4a) for temperature T as a function of depth below the desert surface, z, as shown in Figure 3. The first boundary condition (Eq. 4b) describes heat transfer across the surface layer, undergoing time-dependent solar irradiance and convection, along with diffusion into the ground.[16] The second boundary condition (Eq. 4c) fixes the temperature at a semi-infinite depth, such that:

$$\frac{\partial T}{\partial t} = \alpha \frac{\partial^2 T}{\partial z^2} \tag{4a}$$

$$\begin{aligned} -k\frac{\partial T(0,t)}{\partial z} &= h(T_a(t) - T(0,t)) + R_s(1-\rho) \\ &+\epsilon_a \sigma T_a^4 - \epsilon_s \sigma T(0,t)^4 - (1-\epsilon_s)\epsilon_a \sigma T_a^4 \end{aligned} \tag{4b}$$

$$T(z \to \infty, t) = T_\infty \tag{4c}$$

where α ($\mathrm{m^2\,s^{-1}}$) is the thermal diffusivity, k ($\mathrm{W\,m^{-1}\,K^{-1}}$) is the thermal conductivity, h ($\mathrm{W\,m^{-2}\,K^{-1}}$) is the convective heat transfer coefficient, T_a (K) is the air temperature, R_s ($\mathrm{W\,m^{-2}}$) is the solar radiation flux, ρ is the albedo, ϵ_a is the emissivity of air, ϵ_s is the emissivity of the surface and σ ($\mathrm{Wm^{-2}K^{-4}}$) is the Stefan-Boltzmann constant. All parameters except T_a, h, R_s and ϵ_a are constants. It can be shown that ϵ_a is a function of temperature and can be calculated empirically, as shown in Eq 5.[17] Similarly, h is not constant, but acceptable results are achieved using an assumption of $50\,\mathrm{W\,m^{-2}\,K^{-1}}$, therefore by using data from the CFS climate model[14] for T_a, and using Eq. 6 for R_s,[18] the model can be developed as:

$$\epsilon_a = 0.92 \times 10^{-5} T_a^2 \tag{5}$$

$$\begin{aligned} R_s =& (\tau_b + \tau_d) \cdot R_{sc} \cdot (1 + 0.033 \cdot \cos\frac{2\pi n}{365}) \\ &\cdot (\cos\phi \cdot \cos\delta \cdot \cos\omega + \sin\phi \cdot \sin\delta) \end{aligned} \tag{6}$$

In Eq. 6, τ_b and τ_d are empirical coefficients related to the beam and diffuse radiation respectively, R_{sc} is the solar constant $1367\,\mathrm{W\,m^{-2}}$, n is the day of the year, ϕ is the latitude, δ the solar declination and ω is the hour angle. Note that when the thermodynamic model is used to calculate the low-albedo surface temperature, the subsurface region is modelled as being identical in behaviour to the surrounding soil. In reality, the nature of the construction of the low-albedo surface would influence the temperature profile. However, as this process is unknown, this assumption must be made.

The results of the thermodynamic model compared to the CFS numerical climate model data for average daily temperature at a depth of 5 cm are shown in Figure 5. While the thermodynamic model is consistently overpredicting the temperature, the actual difference is small in absolute terms (mean 1.4 K) and the long-term trend is similar. Clearly, the thermodynamic model is failing to capture some minor effects, however, the temperature is a good approximation, particularly when considering that the thermal mountain effect is driven by the temperature contrast across the low-albedo surface and surrounding terrain, and it is likely that the model will similarly overpredict the low-albedo surface temperature. The CFS dataset could be used to provide sand surface temperature directly, however, if Equation 4 indeed overpredicts the surface temperature for asphalt, using the CFS dataset values will simply artificially increase the temperature contrast, increasing the predicted precipitation. This increase can be substantial, potentially doubling the precipitation output. For consistency, the sand temperatures predicted by Equation 4 were used to evaluate temperature contrast. By using the calculated values for both surfaces, the error is reduced, and the precipitation output more conservative. Within the model, temperature tends to change linearly with albedo when all other parameters are fixed. The parameters of the model are listed in Table 1.

Parameter	Symbol	Value
Thermal Diffusivity ($\mathrm{m^2\,s^{-1}}$)	α	10^{-7}[19]
Thermal Conductivity ($\mathrm{W\,m^{-1}\,K^{-1}}$)	k	0.2[20]
Albedo (sand)	ρ	0.35[4]
Albedo (asphalt)		0.05[21]
Emissivity (sand)	ϵ_s	0.97[22]
Emissivity (asphalt)		0.93[23]
Convective heat transfer coefficient ($\mathrm{W\,m^{-2}\,K^{-1}}$)	h	50

TABLE 1: Fixed parameters of the thermodynamic model

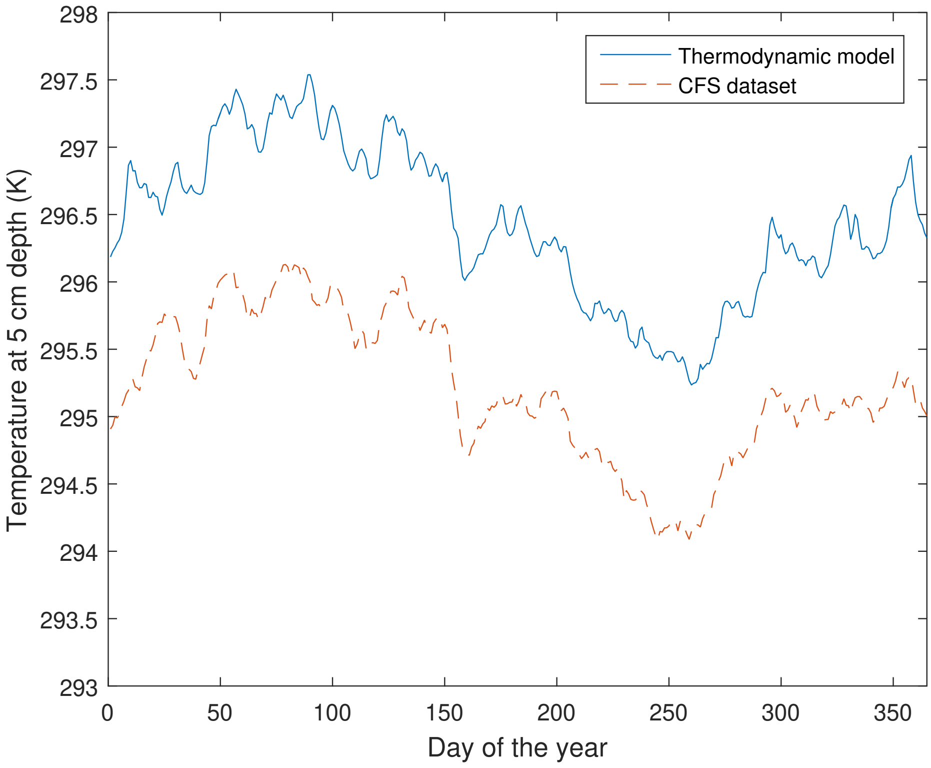

Fig. 5: Comparison of average daily temperature predictions at 5 cm depth for thermodynamic model versus CFS dataset.

3.3 Equivalent Mountains

Previous attempts to model air flow over an isolated island, a problem equivalent to the thermal mountain, have shown that the profile is similar to that of flow over a physical mountain.[24] It is therefore possible to define the equivalent mountain profile that the surface temperature difference creates.[7] The profile is two-dimensional and parallel to the wind. In this analysis, the low-albedo surface is assumed to be rectangular, aligned to have edges parallel to the North-South and East-West lines, and only the component of wind perpendicular to the edge of the box is considered. Therefore the two-dimensional profile can be assumed to be constant perpendicular to the wind along the entire engineered surface. Again, the CFS dataset is used to drive the wind profile. Following the analysis of Black and Tarmy,[7] and from Figure 3, it can be shown that the thermal mountain height $H(x)$ can be approximated by:

If $(\frac{K}{U})(\frac{gs}{U^2})^{\frac{1}{2}} < \frac{1}{2}$ then :

$$H(x) = \begin{cases} 0 & x < 0 \\ \bar{H}\{1 - exp(-\bar{L}x)\} & 0 \leq x \leq L \\ \bar{H}\{exp(-\bar{L}x) \\ \quad \times \Big[exp(\bar{L}L) - 1\Big]\} & x \geq L \end{cases} \tag{7a}$$

otherwise:

$$H(x) = \begin{cases} 0 & x < 0 \\ \bar{H} & 0 \leq x \leq L \\ 0 & x \geq L \end{cases} \tag{7b}$$

where:

$$\bar{H} = \frac{\tau}{sT_a} \tag{7c}$$

$$\bar{L} = (\frac{K}{U})(\frac{gs}{U^2}) \tag{7d}$$

$$s = \frac{\Gamma - \gamma}{T_a} \tag{7e}$$

and where L (m) is the total length of low albedo surface parallel to the flow, τ is the temperature contrast between the sand and low-albedo surface, as calculated by Eq. 4, and shown in Figure 5. Then, Eq. 7e defines a stability parameter s as the difference between the adiabatic (Γ) and environmental (γ) lapse rates ($\mathrm{K\,m^{-1}}$) divided by air temperature T_a (K). K is the eddy diffusivity ($\mathrm{m^2\,s^{-1}}$) of the air and U ($\mathrm{m\,s^{-1}}$) is the wind speed, driven by the CFS dataset. While K is unknown, the term K/U defines the mixing length, which while also unknown, has been shown to have limited influence as the lengths of low-albedo surface approach those considered here, and was approximated as 5 m.[7]

The maximum height of the mountain $\bar{H}$ is defined by Eq. 7c, and is solely influenced by temperature and lapse rates. Regardless of the value of L, the height of the thermal mountain cannot exceed $\bar{H}$. The parameter $\bar{L}$ is defined by Eq. 7d, affected by wind speed and eddy diffusivity, and influences the shape of the thermal mountain profile, but not the height. When K is sufficiently large, or U sufficiently small (therefore a high mixing ratio) Eq. 7a defines the thermal mountain profile, otherwise, the thermal mountain approaches the approximation of Eq. 7b; in practice, however, this approximation only occurs when U is extremely small, and so the moisture flux into the system would be subsequently small and assumed negligible. Therefore, to avoid singularities in the analysis, any cases where $U < 0.5\,\mathrm{m\,s^{-1}}$ were ignored, and the profile taken as flat. An example of equivalent mountain shapes for various values of L can be seen in Figure 6. We note that the analysis assumes a steady state, and that between the hourly timestep of the CFS dataset, the system rapidly approaches this steady state.

3.4 Precipitation Modelling

In order to estimate the precipitation induced by the modified airflow, the equivalent mountain profiles generated by Eq. 7 are used to drive models of orographic, or elevation-induced, precipitation. A simple method to calculate a vertically-integrated source of condensed water per unit time is given by:[25]

$$S(x) = \rho q_v U \nabla H(x) \tag{8}$$

where ρ is the air density (assumed constant at $1.2\,\mathrm{kg\,m^{-3}}$), q_v is the specific humidity (again, driven by the CFS dataset) and ∇H is the gradient of the profile generated by Eq. 7. This does not directly calculate precipitation - further analysis would need to be undertaken to consider the rate of conversion from condensate to precipitate. Therefore, S is simply the mass flux ($\mathrm{kg\,m^{-2}\,s^{-1}}$) and can be converted to precipitation rate via dividing by the density of water ($1000\,\mathrm{kg\,m^{-3}}$), assuming that precipitation conversion is instantaneous. The orographic precipitation model, therefore, calculates the upper boundary of potential precipitation output of the thermal mountain system, and also provides a useful metric to compare the performance of different systems. In order to calculate volumetric water output v ($\mathrm{m^3\,s^{-1}}$), Eq. 8 must be integrated spatially. Noting that the gradient ∇H is the spatial derivative of Equation 7a, and that the other parameters are constant (spatially), the limits $x = 0$ and $x = L$ can be applied and the following equation for v obtained:

$$v = \rho q_v U \int_0^L \nabla H dx \tag{9}$$

Recalling that, except when U is very small, and therefore moisture output negligible, H is defined by Equation 7a, hence Equation 9 can be rewritten as:

$$v = \rho q_v U \bar{H}(1 - exp(-\bar{L}L)) \tag{10}$$

Equation 10 therefore evaluates the volumetric water output at every particular gridpoint from the CFS dataset along the thermal mountain, at each timestep. After the "peak" of the equivalent mountain, $\nabla H(x)$ will become negative, suggesting that the effect would be detrimental to precipitation in the wake of the mountain. As precipitation cannot physically be negative and baseline precipitation is low, only positive values of precipitation between $x = 0$ and $x = L$ where the gradient is positive are used. An example of precipitation output overlayed upon an equivalent mountain profile can be seen in Figure 6. Note that as Equation 8 assumes instantaneous conversion of condensate to precipitate, and instantaneous fallout, this suggests the precipitation would fall on the windward side of the thermal mountain, which may not necessarily be the case in reality.

To obtain the total yearly water output, this must be integrated both temporally and spatially, such that:

$$V = \Big(\frac{1}{2}(v_1 + v_n) + \sum_{i=2}^{n-1} v_i\Big)\Delta y \Delta t \tag{11}$$

where *V* (m^3) is the total volume of water output across the entire system in a single year. Moreover, Δy (m) is the spatial resolution of the CFS dataset (as shown in Figure 7), and Δt is the temporal resolution of the CFS dataset (3600 s). *V* can then be compared to the precipitation target from Section 2 (100 mm yr^{-1} increase across the 1000 km × 2000 km box, equivalent to 2×10^{11} m^3 of water per year) to determine the minimum dimensions of the thermal mountain.

4 OPTIMISING THE THERMAL MOUNTAIN

The model was run simulating the presence of a thermal mountain system along the North, South, East and West edges of the 1000 km × 2000 km box,[4] as shown in Figure 7. The low-albedo surface breadth was modelled as extending the entire edge (again, shown in Figure 7), and the length into the interior of the box varied to find the length that supplied the target precipitation output. Figure 8 and Figure 9 show the results, where, again, the thermal mountain is assumed to be deployed along either the North, South, East or Western edges of the box for comparison. The non-dimensionalised output is shown, where the volume of water output has been divided by the target output to simplify the analysis. The output is different for each edge due to the different in moisture flux and daily temperature fluctuations, driven by the CFS climate dataset. Figure 9 shows the area required to allow for a better

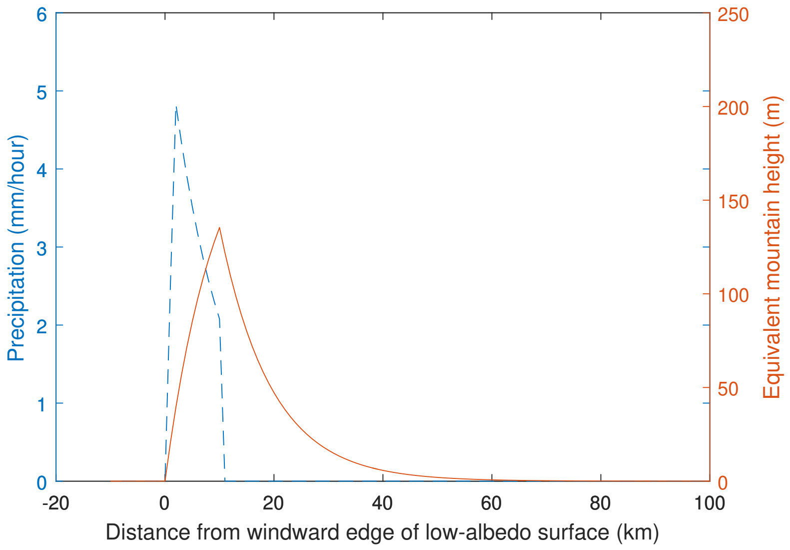

(a) L = 10 km

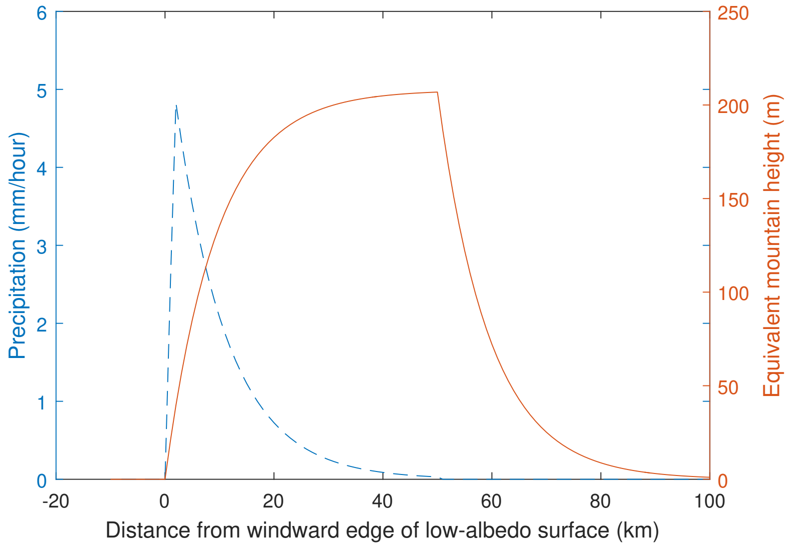

(b) L = 50 km

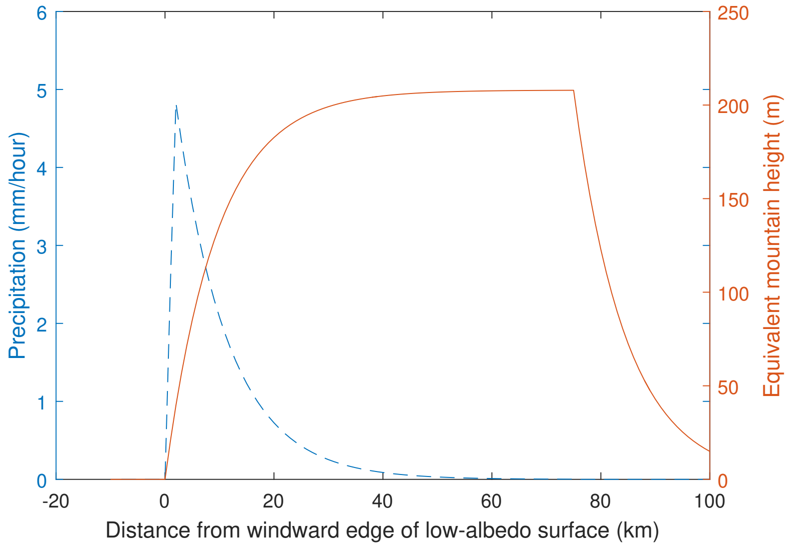

(c) L =75 km

Fig. 6: Precipitation (dashed) and equivalent mountain profiles (solid). L = 10, 50 and 75 km respectively, U = 2.56 m s^{-1}, q_v = 0.0061, T_a = 291 K, τ = 0.85 K

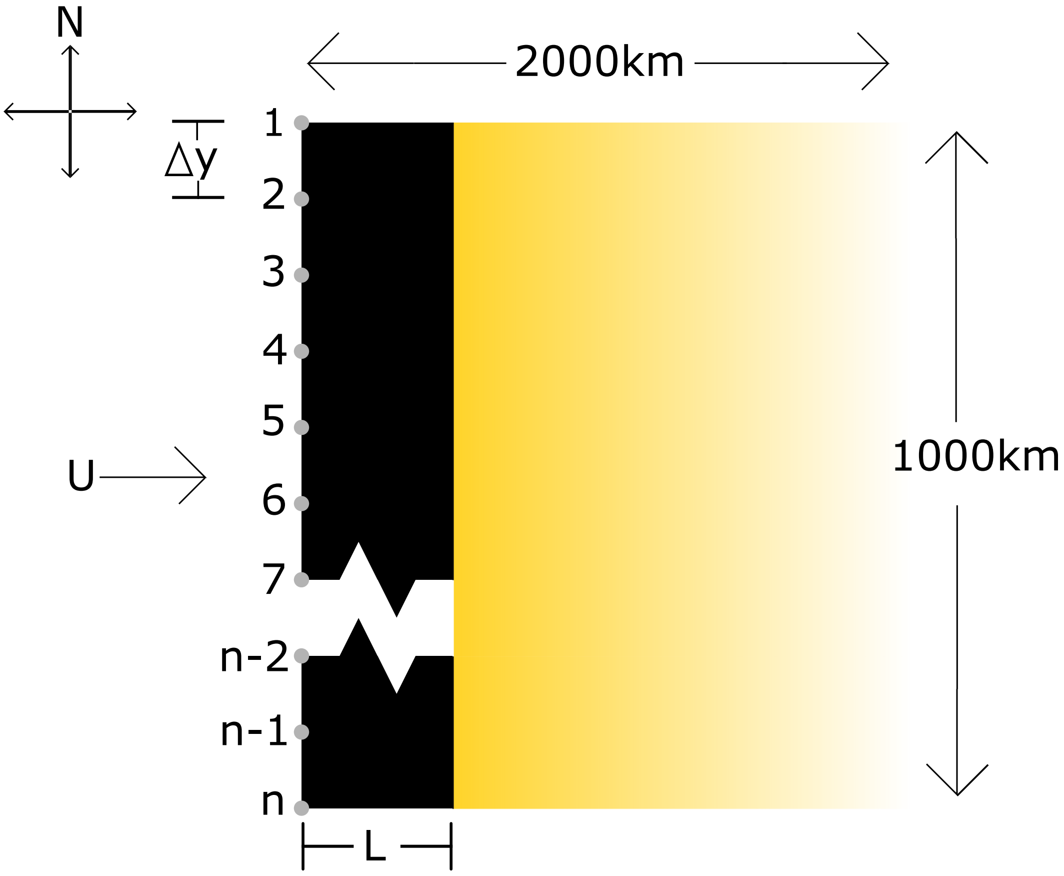

Fig. 7: Schematic of a thermal mountain system existing along the Western edge of the 1000 km $\times$ 2000 km box used by Brovkin et al[4] . U indicates the direction of wind, yellow is the desert interior of the region of interest, black is the low-albedo surface, L is the length of the surface perpendicular to the wind and Δy is the distance between grid points (labelled from 1 to n, where n is the number of grid points from the CFS dataset along the edge of the box).

comparison between thermal mountains across the edges which have different lengths - 1000 km for the systems at the West and East edges, and 2000 km for those at the North and South edges. It can be seen that there is a clear diminishing return and stagnation with increasing values of L. This is due to the exponential decay in Eq. 7a. As x increases, h tends to τ/sT_a, where it stagnates, therefore the system will reach a point where increasing values of L will produce no further positive gradient, and gradient ∇H in Eq. 8 will vanish. This can be seen in Figure 6. The precipitation output increases from L = 10 km to L = 50 km, but thereafter essentially remains unchanged. This creates an argument for a more distributed system, to lessen the impact of diminishing returns and stagnation.

It is now possible to perform a simple analysis of a combined system deployed along several edges, however, modelling more complex geometries, such as alternating strips of desert and low-albedo surface, would be more difficult, as in the current model, each successive thermal mountain would not consider the humidity removed from the atmosphere by the previous. A full numerical simulation would

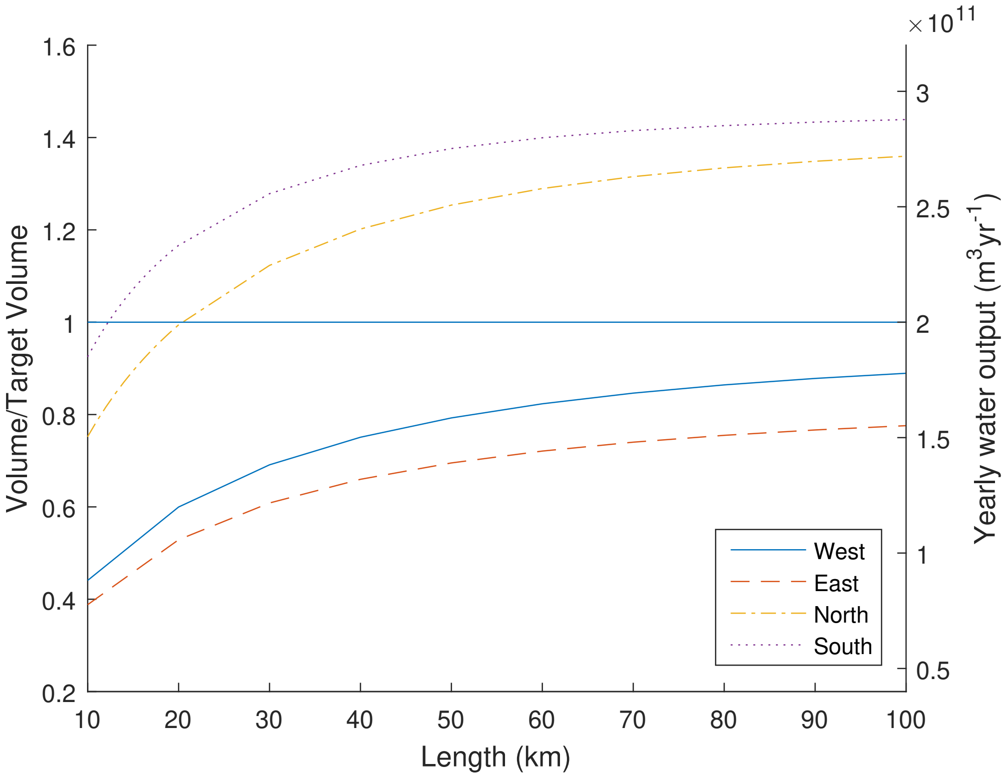

Fig. 8: Engineered surface length versus volumetric water output for a thermal mountain deployed along each edge of the $1000\,\text{km} \times 2000\,\text{km}$ box

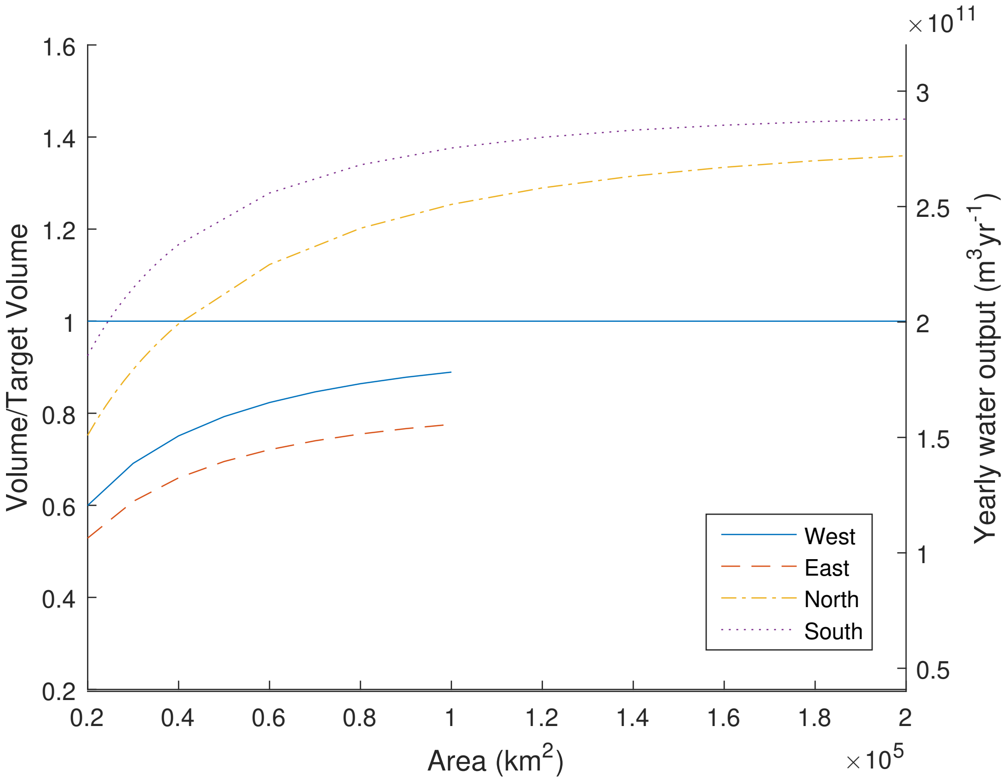

Fig. 9: Engineered surface area versus volumetric water output for a thermal mountain deployed along each edge of the $1000\,\text{km} \times 2000\,\text{km}$ box

be more suited to modelling such a system.

The results for the thermal mountain output when deployed along each edge can be modelled via a least-squares curve fit of the form $V = \alpha ln(L) + \beta$, where V is total yearly volumetric precipitation output and L is the length extending inwards from the edge of the box. It is now possible to find the optimal low-albedo surface area for a combined system deployed along two edges in order to minimise the thermal mountain area for a given required precipitation output. If B is the breadth (1000 km for thermal mountains at the West and East, and 2000 km for North and South edges, shown in Figure 7) and L the length extending inwards from the edge of the box for a particular edge, the optimal value of L can be obtained as:

$$L_1 = \left(\frac{B_2}{B_1}\frac{\alpha_1}{\alpha_2}e^{\frac{1-\beta_1-\beta_2}{\alpha_2}}\right)^{\frac{1}{\frac{\alpha_1}{\alpha_2}+1}} \tag{12}$$

which minimises the total surface area for a given precipitation output. The indices denote one of the two edges being considered; to obtain the second length, the equation is identical, but with the indices reversed. For the derivation of this result, see the Appendix. The parameters for each edge can be found in Table 2. Due to the diminishing returns with increasing L, it is more efficient in terms of total surface area to utilise two thermal mountains on different edges. Similar results can be derived for 3 or 4 edges, with further increasing efficiency. However, these approximations do not consider the possibility that the removal of moisture from the atmosphere at one edge may have a significant impact upon the available moisture at the others.

In order to examine the concept on quantitive scales, the area and mass of material required for various configurations can be calculated and is shown in Table 3. It can be seen that thermal mountains deployed along the South and West edges of the box minimise the total thermal mountain area. Again, this is driven by the moisture flux and climate conditions from the CFS dataset. Due to the diminishing returns of increasing length, thermal mountains solely along

Edge	α	β
North	0.2857	-1.8683
East	0.1683	-1.1399
South	0.2823	-1.6933
West	0.1953	-1.336

TABLE 2: Parameters for least-squares fit to model output

the East and West edges reach the target output at extremely large areas and were therefore omitted. However, their contribution as a joint system can still be considered. To provide a baseline estimate, a low-albedo asphalt coating will be assumed, although a large range of coatings could be considered. While asphalt mixtures can vary, its density is taken as $2360\,\mathrm{kg\,m^{-3}}$. Estimating the required asphalt depth is difficult, as while, for example, asphalt roads can vary in depth, these are load bearing structures and the application of an asphalt coating for creating a thermal mountain could be significantly thinner. A depth of 50 mm was assumed. As can be seen, even the most efficient deployment of a thermal mountain system across the Western and Southern edges requires truly vast quantities of material, of order 1.8×10^{12} kg. As a comparison, the concrete output of China between 2011 and 2013 was 6.6×10^{12} kg,[26] so a project of this order of magnitude, while vast, is not entirely implausible. It is also worth noting that the mass required scales linearly with the necessary depth, which could be significantly less than the assumed 50 mm. Enhanced rock weathering, proposed as a solution to increasing atmospheric CO_2, would require the deployment of between 1 and $5\,\mathrm{kg\,m^{-2}yr^{-1}}$ across an area of 20×10^6 km, or 1 to $5 \times 10^{12}\,\mathrm{kgyr^{-1}}$.[11] This is an application of mass of order of magnitude equal to the thermal mountain every year.

5 MODEL SENSITIVITY

The model presented provides a top-level systems engineering assessment of requirements for a thermal mountain system by coupling a heat transfer and precipitation model to climate simulation datasets (CFS data). However, the model is limited by a number of assumptions. These include degradation of the system's performance, such as induced clouds blocking out sunlight, thereby lowering the temperature contrast of the surface coating and inhibiting the thermal mountain effect. Also, the model is driven by air temperature data from the CFS climate

Edge(s)	Area ($\mathrm{km^2}$)	Mass (10^{12} kg)
North	45800	6
South	27800	3.7
North and East	20400	2.7
East and South	14800	1.9
South and West	13700	1.8
West and North	18500	2.4

TABLE 3: Area and mass requirements for different locations of thermal mountain

model, which could be modified by the presence of the thermal mountain itself, lowering the stagnation height of the equivalent mountain. However, such feedback effects could also could manifest in positive ways, such as thermal updrafts drawing more air towards the low-albedo surface, thus increasing precipitation output. Such coupling could be better modelled by finite element analysis, and will be considered in future studies. The model also offers no indication of the wider impact of removing moisture from the atmosphere at one area, which could lead to reduced precipitation in another. The use of a numerical climate model, operating on a global scale would be required to investigate this issue further.

The analysis considers the precipitation necessary to irrigate the $1000\,\text{km} \times 2000\,\text{km}$ box simultaneously. However, it may be possible to locally irrigate areas on a much smaller scale, closer to the thermal mountain, and the induced vegetation would provide its own contribution to inducing rainfall through lowered surface albedo and increased roughness.[4] It may, therefore, be possible to induce the tipping point to a vegetated state through much smaller interventions, through the spatial diffusion of vegetation away from the initial thermal mountain. This paper bases the target precipitation around the precipitation-vegetation interaction model developed by Brovkin et al, which applies only on a macroscopic scale. The use of the simple upslope model in Eq. 8 also likely overpredicts precipitation, and accuracy is further lost by assuming key environmental variables as constants. The influence of these variables and introduction of a precipitation efficiency will now be investigated.

5.1 Precipitation Efficiency

It can be seen that Eq. 8 is a measure of the maximum precipitation potential. If precipitation efficiency is defined as λ ($0 \leq \lambda \leq 1$), Eq. 8 scales as:

$$S(x) = \lambda \rho q_v U \nabla h(x) \tag{13}$$

which corresponds to an adjusted trendline of $V = \lambda(\alpha ln(L) + \beta)$. Therefore, from Eq. 12, calculating the dimensions for a combined thermal mountain system along two edges, yields:

$$L_1 = \left(\frac{B_2}{B_1}\frac{\alpha_1}{\alpha_2} e^{\frac{\frac{1}{\lambda} - \beta_1 - \beta_2}{\alpha_2}}\right)^{\frac{1}{\frac{\alpha_1}{\alpha_2}+1}} \tag{14}$$

Figure 10 shows the required area for the North-West edge combined system to achieve the target precipitation output as a function of the precipitation efficiency. Precipitation efficiency is likely to be strongly dependent on local conditions and therefore highly variable, however, this does demonstrate its key importance. As precipitation efficiency lowers, it linearly increases the necessary vertical water flux. Since the output of the system exhibits diminishing returns and stagnation with increasing length, a decreasing precipitation efficiency exponentially increases the area of low-albedo terrain required, as can be seen from scaling of Equations 13 and 14.

5.2 Effect of mixing length and environmental lapse rate

In Section 4, the model was evaluated with the environmental lapse rate fixed at $5.7\,\mathrm{K\,km^{-1}}$ and a mixing length of 5 m, in accordance with earlier studies.[7] The model is now evaluated at extreme values for these key parameters, ranging from $1\,\mathrm{K\,km^{-1}}$ to $7\,\mathrm{K\,km^{-1}}$ for the environmental lapse rate[27] and 0.15 m to 30 m for the mixing length.[7] The results for this analysis, considering a thermal mountain deployed at the Southern edge, can be seen in Figure 11. As can be seen, when either of these values are at the lower extreme, the output either saturates far below the precipitation target, or fails to approach it at any reasonable scale. However, when both are at the upper extreme, the output very rapidly reaches the target output at approximately 2 km length extending into the box. This highlights the dependence of the model on these parameters, which are highly variable, dependent on environmental conditions and difficult to predict. However, the parameters used in Section 4 are appropriate for the systems engineering analysis of this paper.

6 IRRIGATION AND AGRICULTURAL APPLICATIONS

A smaller scale deployment of the thermal mountain effect has potential applications in agriculture. The use of the precipitation output as part of an irrigation system in the Sahara is now investigated, along with a potential irrigation and water transport strategy. Such an irrigation scheme would also be required to initiate the diffusion of vegetation on a larger scale for carbon sinks.

6.1 Water demand

Maize grown in Egypt requires a total of 653.4 mm of irrigation per year, including runoff and evaporative losses.[28] Using the assumption that the climate and soil is

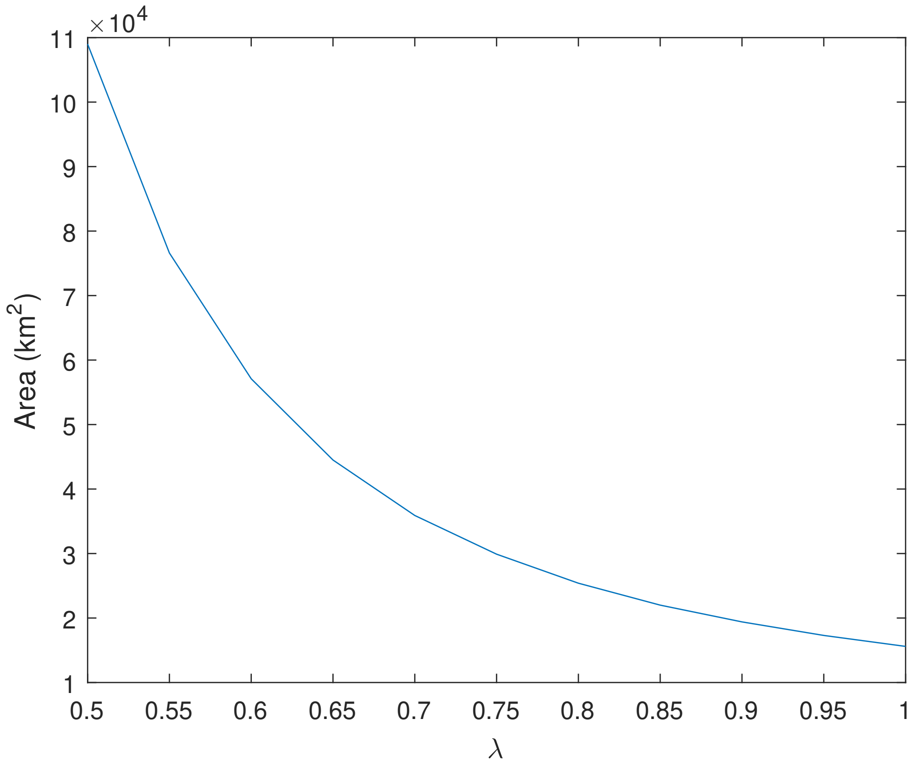

Fig. 10: Required low-albedo surface area to achieve target output of combined North-West system as a function of precipitation efficiency

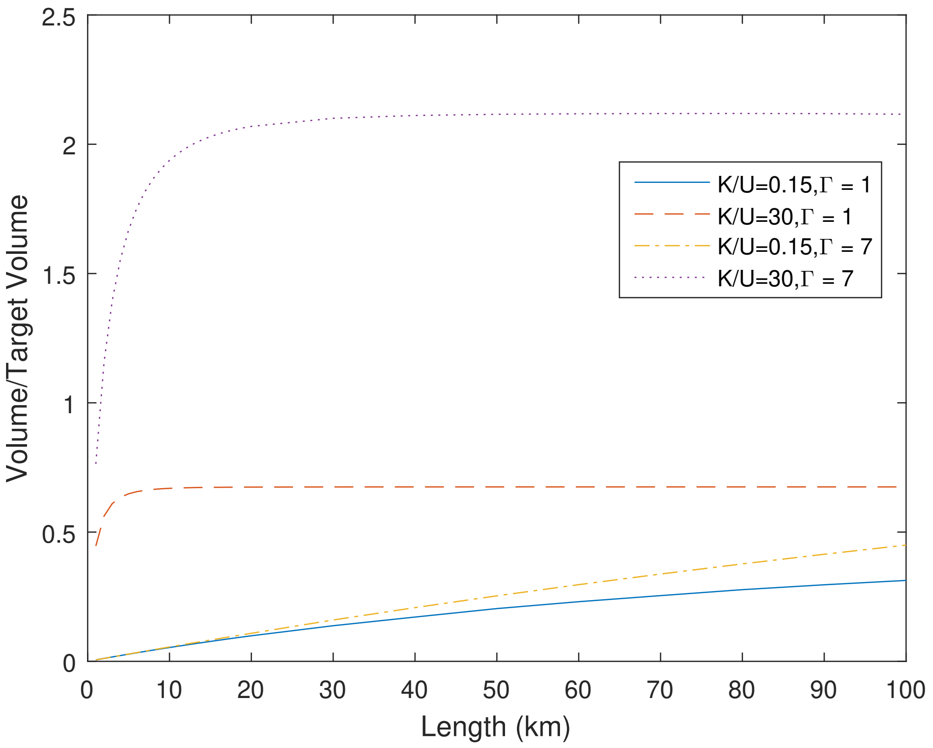

Fig. 11: Model results for a low-albedo surface along the Southern edge of the box for extreme values of mixing length and environmental lapse rates

not so vastly different to render this figure invalid for the Sahara, it is possible to assess how much land a thermal mountain system could irrigate. On average, the volumetric water output of a thermal mountain system deployed along the South edge with a length of 16 km (the maximum length before stagnation of precipitation output) is approximately 100 000 m^3 of water per unit breadth (m) per year, therefore, such a system would provide sufficient water to irrigate 153 046 m^2 of maize fields per metre breadth, or a ratio of asphalt to irrigated area of 1:10.

6.2 Irrigation Strategy

The simple upslope precipitation model predicts that most of the precipitation will occur over the thermal mountain itself. While this will be influenced by precipitation conversion and fallout times and may be downwind of the engineered thermal mountain surface, any large-scale application of the concept must also consider the transportation of this water. In order to utilise the precipitation, it would firstly need to be captured. The thermal mountain system could be constructed on a gradient leading into a reservoir, or the entire structure could consist of a grating, where the slots in the structure were angled such that the low-albedo surface absorbed the solar radiation, but provided a means for water to drain into a reservoir below. Regardless of how this could be achieved, the water would then need to be transported across large distances if it were to be used in agricultural applications, or for large-scale afforestation.

In a desert environment, where evaporative loss is an issue, a likely method of irrigation would be a centre pivot system, where a system of suspended sprinklers upon an arm rotates slowly around a centre pivot, applying water to circular areas of approximately 50 ha. These systems have previously been deployed in the Sahara and can have evaporative losses of between 3 and 5 % in arid climates.[29] Transporting water to these irrigators is a non-trivial problem with substantial room for optimisation, however, a simplified analysis can provide an order-of-magnitude estimate for the power requirements of such a system. If the thermal mountain along the Southern edge of the 1000 km × 2000 km box is considered, and the irrigators are assumed to extend out from the edge into the interior of the box, fundamental hydraulic equations can be combined with parameters from existing canal and irrigation systems to calculate the head required to transport the water from the thermal mountain to the irrigators, and subsequently, the power requirements. Two variations on such a system could exist - one where a smaller main reservoir exists and the canals move the water slowly throughout the year, with larger dispersed reservoirs to hold the water between growing periods, or a larger main reservoir, from which water is pumped at a greater rate only during the growing period. This also, therefore, assumes that the thermal mountain system has been deployed for long enough to accumulate sufficient water that the output can be considered constant, with reservoirs acting as buffers. Further considerations would include land fertility, local climate conditions, suitability of the terrain for building both water infrastructure and infrastructure for importing and exporting resources. A schematic of the proposed concept is shown in Figure 12. The following analysis estimates the power requirements of moving sufficient quantities of water to maize fields, based upon the irrigation requirements discussed in Section 7.1. The analysis assumes rectangular concrete prismatic canals of uniform gradient, no water losses in the transport system and flat terrain. In reality, there would be inherent losses in the canal and terrain obstacles would complicate the problem. The irrigated areas are assumed to be circular, but packed together in squares. While augmentations to the centre pivot system can allow for irrigated squares, and circles can be packed together more efficiently, it is assumed that practically there would need to be empty space left for infrastructure, therefore one irrigator of arm length r and irrigated area πr^2 occupies an area of $4r^2$. Under the proposed concept, the canal runs between the irrigators, supplying water to a reservoir which provides the pressurised flow to four surrounding irrigators, with the remaining water is transported onwards to the next irrigator.

The velocity of water flowing in an open channel at steady state can be taken as:[30]

$$U_c = \frac{1}{n} R^{\frac{2}{3}} \sqrt{s_f} \tag{15}$$

where U_c is the velocity of the water ($\mathrm{m\,s^{-1}}$), n is the Manning coefficient, R (m) is the hydraulic radius (defined as the ratio of the cross sectional area to the wetted perimeter) and s_f is the gradient of the slope. This would also be the ratio of the hydraulic head provided by the pump to the length of the canal, if the start and end were on the same elevation. A larger canal section would allow for the same volumetric flow for a given head, but the construction costs of the canal would

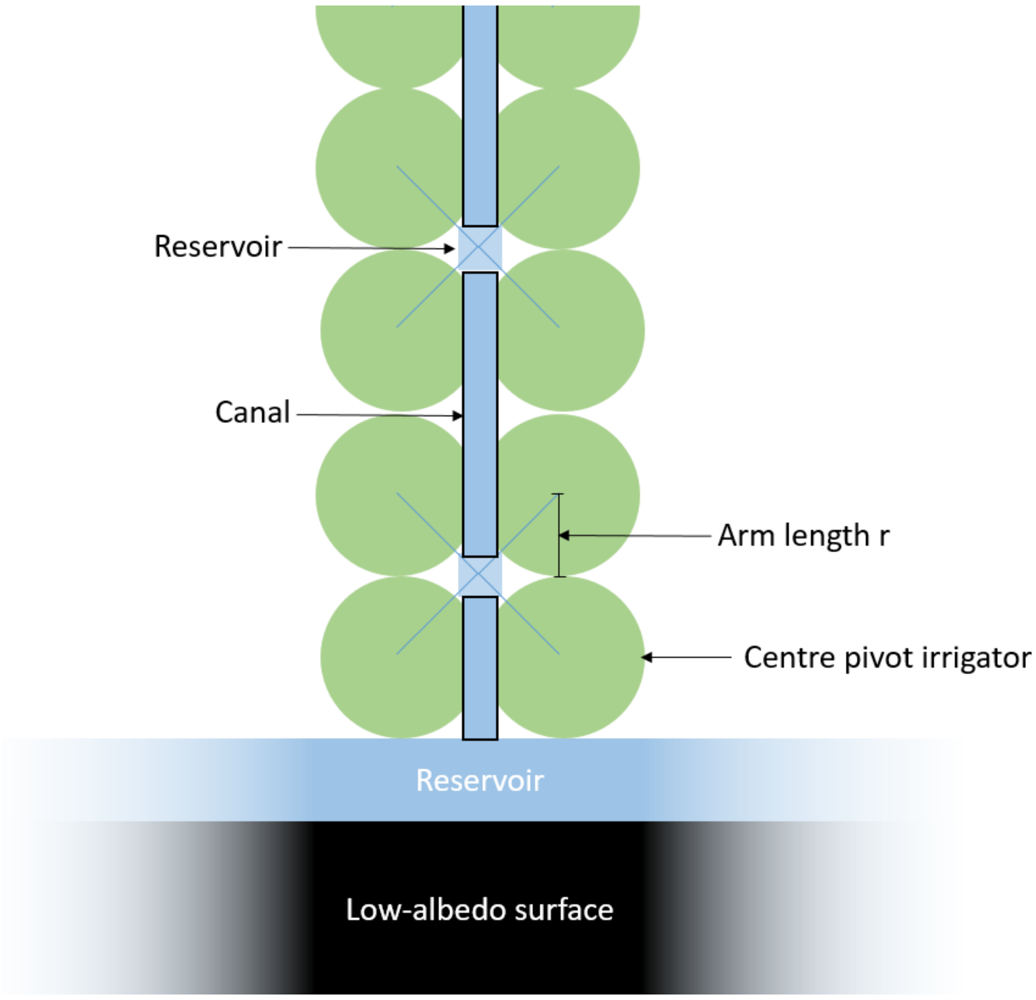

Fig. 12: Schematic of potential irrigation infrastructure.

be increased, and possibly maintenance costs would offset the savings in power consumption. To reduce the number of variables, the canal sections were designed such that their width is equal to twice the depth of water, as this is the lowest wetted perimeter possible for a rectangular canal. By using this assumption in Eq. 15, along with volumetric flow rate, $Q = AU_c$, a relationship for the required width of canal can be found:

$$W = \left(\frac{4Qn}{\sqrt{s_f}}\right)^{\frac{3}{8}} \tag{16}$$

where W is the width of the canal (m). This analysis would allow the approximate design of canal sections for carrying water between reservoirs, and the power costs for doing so. From the smaller reservoirs, the water could be carried in pressurised pipes to the centre pivot irrigators. Head requirements would be calculated as:[29]

$$H = \frac{U_w^2}{2g}\frac{fL_p}{D} + \frac{P_p}{\rho g} + H_s = \frac{8Q^2 fL_p}{g\pi^2 D^5} + \frac{P_p}{\rho g} + H_s \tag{17}$$

where H is the head requirement (m), U_w is water velocity (m s^{-1}), g is the gravitational acceleration (m s^{-2}), L_p is the length of the pipe, or the distance between the pivot irrigator and the reservoir (m), D is the pipe diameter (m), P_o is the operating pressure of the irrigator, ρ is the density of water (kg m^{-3}), H_s is the height of the sprinklers above the ground and Q is volumetric flow rate (m^3 s^{-1}), calculated by multiplying daily irrigation by area and dividing by 22 hours, a typical operating period for centre pivot irrigators.[29] Losses from water travelling along the arm of the irrigator are difficult to estimate, however, as the length of the arm is approximately 400 m and flow rate decreases along the length of the arm, so the loss will be small compared to the losses in the main pipe, and are therefore assumed negligible. Finally, f is the friction factor, defined by:[29]

$$f = \frac{0.316}{Re^{1/4}} \quad Re = \frac{UD}{\nu} \tag{18}$$

where Re is the Reynolds number and ν is the kinematic viscosity (m^2 s^{-1}).

With this analysis, it is possible to calculate power requirements for a water transport scheme of this scale, based on the system of main canals and pressurised pipelines from central reservoirs. However, even with the assumption of homogenous terrain and fertility, there are still a number of design parameters, such as number of main canals and reservoirs, which in reality would be determined through consideration of a range of issues. As optimisation of a water delivery network is not the focus of this paper, these parameters are chosen based around existing systems. A true implementation of water infrastructure on this scale would likely be different, however, this analysis provides an engineering estimate as to the power requirements.

As discussed previously, each meter of a 16 km length thermal mountain can provide water for 153 046 m^2 of maize fields. A typical arm length of a centre pivot irrigator is 400 m,[29] meaning a 16 km by 800 m (twice the pivot radius) thermal mountain will provide water for approximately 244 adjacent irrigators, extending 195 km into the desert. Since this analysis is of a canal running between two rows of irrigators, the analysis will be for each 1.6 by 16 km area of low-albedo surface, supplying water to 488 centre pivot irrigators, and irrigating 245 km^2 of maize fields. There would be room for 1250 such systems along the Southern edge of the desert box. At each stage of the canal, the water to be carried to subsequent stages is given sufficient head to carry it at the designated flowrate to the next reservoir.

If a constant gradient is assumed, then the head requirements at each subsequent reservoir will be the same (equal to gradient s_f multiplied by length between the reservoirs), but the canal width and power consumption will be lowered. The power requirements are calculated as:[30]

$$P = Q\rho g H \tag{19}$$

The water flow rate (m^3 s^{-1}) at any stage in the canal can be defined as:

$$Q(n_y) = Q_T(1 - \frac{n_y - 1}{N_y}) \tag{20}$$

where Q_T is the total water output of the thermal mountain system m^3 s^{-1}, N_y is the number of subreservoirs and n_y is the number of subdivisions the main canal has passed at that particular position along the overall canal.

The distance between each reservoir will be 800 m (twice the arm length), save for the first and last, which would be 400 m. Taking the gradient as a constant 0.00012 (a gradient used by sections of the California Aqueduct[31]), the head requirements at each stage can be calculated as the gradient multiplied by the length. This means the head requirements will be identical at each stage, save for the first and last, since they have half the length. The power requirements can then be calculated using Equation 19. The summation of the power consumption of the individual stretches of canal represent the total power consumption of the overall system, given by:

$$P_{Tc} = \Big(\sum_{i=2}^{N_y-1} Q(i) + \frac{1}{2}(Q(1) + Q(N_y))\Big)\rho g H \tag{21}$$

Under the assumption of constant flow throughout the year, power consumption was calculated as 578 kW per canal. The widest canal section would be between the main reservoir and the first subreservoir, requiring a width of 3.3 m. Every subsequent canal would be smaller, as determined by Equation 16. If the flow is taken solely during the 86 day growing period, the power consumption is significantly higher at 2453 kW (a yearly energy consumption approximately four times as large as the year-round flow case), with a maximum canal width of 5.7 m.

The power consumption to supply the pressurised water to the irrigators can be computed similarly, making the assumption that the pipe diameter is 0.25 m. Using Equation 17, where L_p is the length from the central reservoir to each of the irrigators it serves ($L_p = \sqrt{2r}$), and Q being the flow rate for an individual irrigator, then multiplying by the total number of reservoirs. The power requirements for the centre pivot irrigators would vary throughout the growing season, but at the average of 7.6 mmday^{-1},[28] the power consumption for all irrigators surrounding one canal would be 1455 kW. Note that this is only the power required to supply the pressurised water, and not to rotate the irrigation equipment around the pivot.

7 CARBON SINKS

Through its potential to transition desert land into a vegetated equilibrium state, the thermal mountain effect could be used in conjunction with eucalyptus plantations as large-scale carbon sinks, as considered by Ornstein et al.[5] This would directly sequester carbon, and the altered surface albedo and roughness of the vegetated land would further contribute to tipping the desert into the vegetated state. Eucalyptus trees are effective carbon sinks, and their biomass production can be enhanced through effectively fertilised and managed plantations.[33]

A field study assessed the resource use of eucalyptus plantations in Brazil. The forests contained trees between the ages of 5 and 8 years and were planted in approximately 3.5 m×2.6 m grids, which is approximately 1000 trees per hectare. The productivity of the forests ranged from an above-ground net primary productivity (ANPP - total biomass production per area per time) of 10.9 Mg ha^{-1}yr^{-1} for low-productivity strains to 27.5 Mg ha^{-1} yr^{-1} for higher productivity strands. The moderate-productivity strands had an ANPP of 16 Mg ha^{-1}yr^{-1}, with yearly rainfall of 1000 mm yr^{-1}.[34] As approximately 50% of this biomass is carbon,[35]

Parameter	Symbol	Value
Total output ($m^3 s^{-1}$)	Q_T	6342
Manning coefficient ($sm^{-1/3}$)	n	0.013[30]
Gradient	s_f	0.00012[31]
Pivot radius (m)	r_p	400[29]
Pivot discharge (pressure kPa)	P_p	55[32]
Sprinkler height (m)	H_s	0.6[32]
Pipe diameter (m)	D	0.25

TABLE 4: Values used in calculation of water infrastructure

this equates to 0.8 kg m^{-3} (mass of carbon per volume of water). The moderate-productivity strain will be considered for the following analysis.

Figure 13 shows an estimate of the potential for carbon capture and irrigated eucalyptus forest areas as a function of low-albedo surface area for each of the edges of the 1000 km × 2000 km box, used by Brovkin et al.[4] Global CO_2 emissions in 2015 were 3.6×10^{13} kg CO_2,[36] or 9.9×10^{12} kg of carbon. Figure 13 also shows that a thermal mountain deployed at the South of the box would only be sufficient to offset global carbon emissions by around 2%. This is in contrast to the analysis of an irrigated Sahara by Ornstein et al,[5] where a fully irrigated Sahara (an area of 9.8×10^6 km^2, about 5 times the area of the 1000 km × 2000 km box) is proposed to offset emissions entirely. However, Ornstein et al consider an entirely irrigated Sahara, using approximately 20 times the water output of a stagnated thermal mountain. They further assume that high-efficiency irrigation is used, which halves the water consumption of the eucalyptus trees, and further, the figure used for ANPP of the trees is increased by 20% due to underground carbon. With the latter two assumptions, the use of thermal mountains to provide sufficient carbon sinks to offset global emissions becomes more feasible (under the same assumptions, the 2% offset would increase to around 5%). Further, the 2% drawdown is using direct irrigation of eucalyptus plantations, not considering feedback effects, including evapotranspiration returning water to the environment. More extensive modelling using the CFS dataset over the entire Sahara, or using climate models directly modelling low-albedo surfaces, would be necessary for a better comparison between artificial thermal mountains and direct desalination-irrigation. However, rather than being seen as a direct alternative to desalinated water-driven irrigation, deployment of thermal mountains could be used to enhance desalination, and lower the vast power requirements of the system, estimated at around 4500 nuclear plants.[5]

8 DISCUSSION

The model shows that the scale of material inputs required to achieve target precipitation is potentially vast. It is therefore necessary to investigate methods of reducing the scale of intervention to vegetate the 1000 km × 2000 km box. This could be achieved by refining the original concept, such as reducing the necessary depth of asphalt, or using an alternative low-albedo material, such as a black plastic

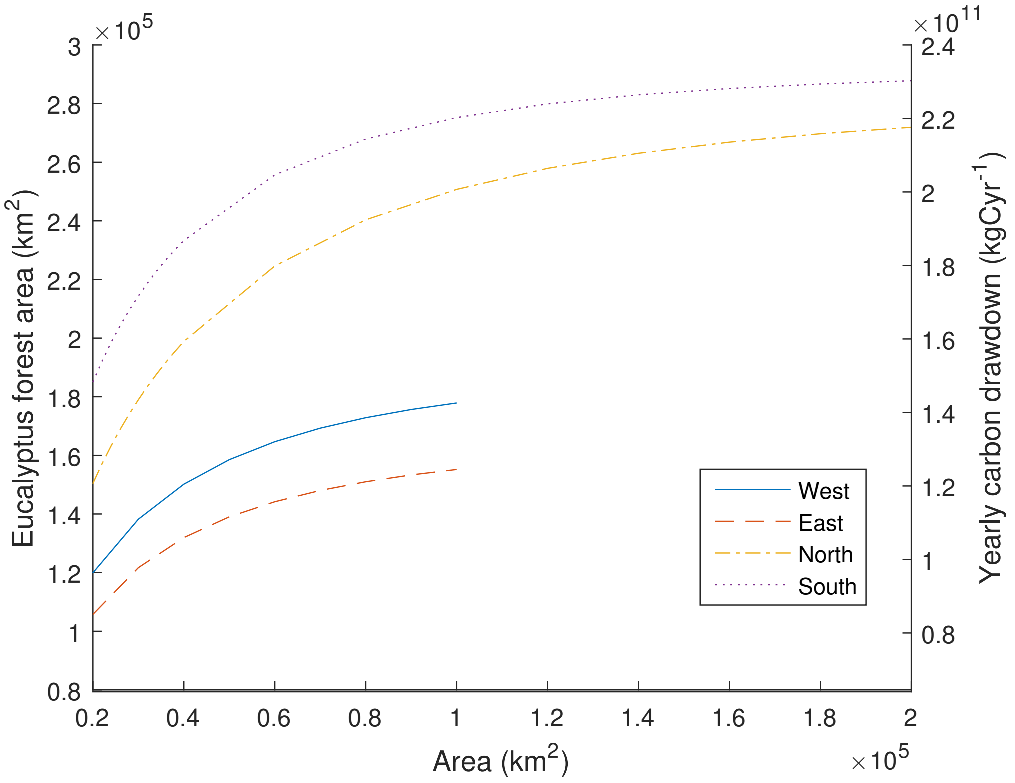

Fig. 13: Potential carbon drawdown and eucalyptus forest area as a function of low-albedo surface for each respective edge of the 1000 km × 2000 km box

membrane, to achieve the same effect. The model also only calculates the output based on asphalt strips running parallel to the edges of the box. It is possible that a more effective deployment would be achieved by deployment in regions with high moisture flux across the boundaries, and where high temperature contrasts were achieved. This will be investigated later, in Section 8.2.

As has been discussed earlier, there are a number of simplifications made to the model which were deemed appropriate due to its low-order nature. The use of the CFS climate data makes the assumption that the engineering intervention will not substantially affect these parameters. The thermodynamic model makes a number of assumptions, primarily that some of its driving parameters, such as local albedo, remain constant and fixed across the area of interest. These assumptions are deemed acceptable given the verification against the CFS dataset. Modelling the airflow again makes assumptions of some environmental parameters, along with the assumption that the system very rapidly reaches steady state across timesteps. The precipitation model makes fewer assumptions due to its simplicity, although as discussed in Section 3.4, it is only calculating the maximum possible precipitation. In Sections 6 and 7, two scenarios are laid out discussing applications of the thermal mountain effect. Both of these scenarios involve a number of design assumptions, as covered in the respective sections, as an in-depth analysis of these were not the primary focus of this paper.

There are, however, some other assumptions not previously discussed, which would have implications upon the engineering of thermal mountains. Firstly, if asphalt is used, it will require maintenance. The dark surfaces being covered by sand or growth of organisms due to increased precipitation will diminish the thermal mountain effect, and require continuous maintenance to ensure the albedo is kept low. This means that at least some of the surface must be road suitable for maintenance vehicles, which themselves require maintenance and infrastructure. Analysing these additional issues is beyond the scope of this study, however, there are a great number of additional considerations to be made.

Similarly, beyond approximate water requirements, the type of vegetation has not been considered as an engineering consideration for the system. Vegetation will impact the system in a number of ways, such as suitability of terrain, vegetation roughness and albedo, and competition with other plantlife.

8.1 Alternate Concepts

There are several variations on the thermal mountain concept worthy of investigation. These include the use of heat capacitors buried underneath the low-albedo surface to prescribe a degree of controllability and therefore optimisation of the transient temperature profile of the surface. In principle, this could amplify the thermal mountain effect when favourable conditions are predicted. Similarly, replacing the low-albedo surface with solar panels can be considered, whereby waste heat from the panels would create a thermal mountain, and the power could either be used to power desalination plants as a hybrid with conventional irrigation, or to store energy and heat the surface and so create a thermal mountain when direct solar energy is insufficient. Performance could also be increased by supplying the low-albedo surface with a thin film of seawater. The heat would drive evaporation as well as desalination, similar to a concept for humidifying air in coastal areas with floating devices that attract a thin film of seawater.[37]

The solid low-albedo surface could also be substituted with the application of dark powder, such as biochar. Biochar is a obtained from processing biomass, and is essentially pure black carbon in a powdered form. It is chemically stable, and therefore has the potential to store carbon sequestered from the air, and it is also known to increase soil fertility.[38] Biochar is created via pyrolysis of biomass, and the syngas by-products can be used in the creation of biofuel and ammonia, a key component in fertiliser.

One can imagine a scenario in which vegetation is grown in arid land, either through conventional means or taking advantage of the thermal mountain effect, then selectively harvested in order to facilitate the production of biochar and fertiliser. These resources could then be used to expand the thermal mountain, producing a positive feedback effect. This concept has a number of advantages over a conventional thermal mountain, such as the construction of the thermal mountain utilising locally-sourced resources. It also circumvents the need for an extensive irrigation system, as the majority of the rainfall is over the peak of thermal mountain, where the ground would be most fertile. A disadvantage would be that the biochar would likely need regular replenishment, as winds would mix the biochar with sand. However, this would also present opportunities for continuous, long-term burial of carbon.

Some rocks used in rock-weathering, such as basalt, are dark, therefore, some of this discussion will apply similarly. One can imagine a scenario where basalt dust is deployed to achieve both rock-weathering and the thermal mountain effect.

8.2 Moisture flux and temperature contrast

The results in Section 4 show that a thermal mountain located along the South edge of the $1000\,\mathrm{km} \times 2000\,\mathrm{km}$ box is optimal in the use of land area to provide necessary irrigation, with the North being second most effective location. This is partly due to the geometry of the problem - the North and South edges have twice the length, therefore twice the scale for humidity input. As discussed, increasing L has diminishing returns, and the increased overall moisture flux allows the North and South edges to reach the target precipitation further from the equivalent mountain stagnation height of τ/sT_a. However, this is not the sole reason. Figures 14-17 show the mean values of absolute moisture flux and temperature contrast for each edge, against the CFS climate model grid point positions and the day of the year. In Figure 15, it can be seen that the West edge has relatively high moisture flux, and it may then be assumed that this would make it the optimal location for a thermal mountain system, whereas in fact the model results show that it is the worst. Figures 16 and 17 show that the West edge generally has lower a temperature contrast than the other edges, meaning that despite the high moisture flux, less of it is driven upwards through convection, and therefore has lower precipitation output. Conversely, the South edge generally has much higher temperature contrast, giving a higher precipitation rate despite the lower moisture flux. The temperature advantage is likely due to the higher solar irradiance, where all grid points are at the closest to the equator.

This raises interesting questions regarding deployment of a thermal mountain system. For example, if the moisture flux and temperature contrast were generally consistent over a long timescale, it would be more efficient to create low-albedo terrain across sections of the edges with high temperature contrast and moisture flux. If a more temporary method of albedo alteration were used, such as deployment of biochar, it would be more efficient to focus on different areas at different times of the year. The areas of high moisture flux but low temperature advantage again raise an interesting concept for the thermal mountain using stored energy, where the surface is artificially heated when favourable conditions are predicted. An investigation would be required to determine whether it is more energy efficient to heat areas of lower temperature contrast, but high moisture flux, or to further increase a higher temperature advantage where the moisture flux is lower.

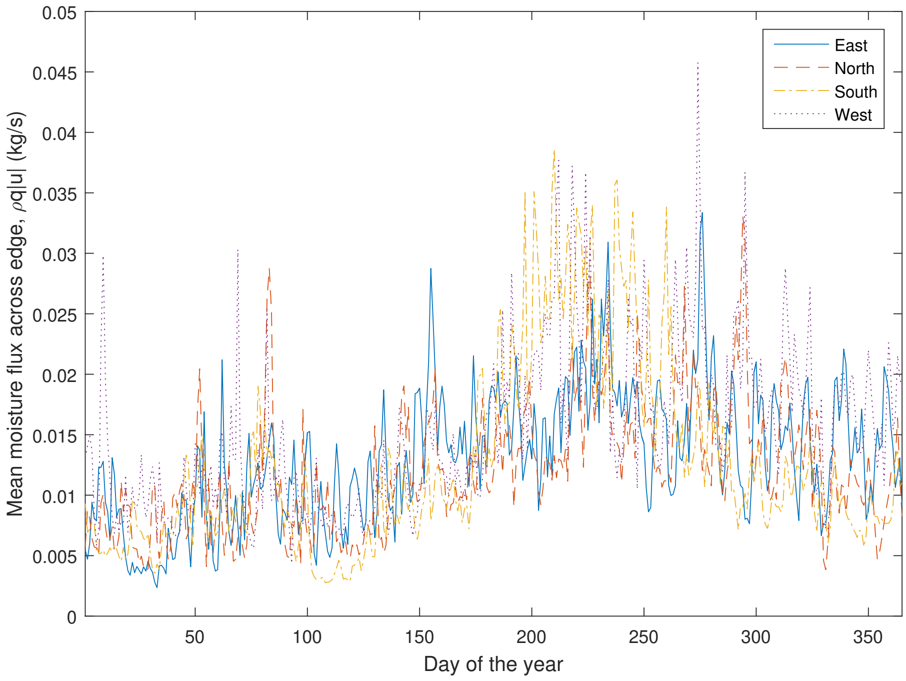

Fig. 14: Mean daily moisture flux over the entire year across each edge

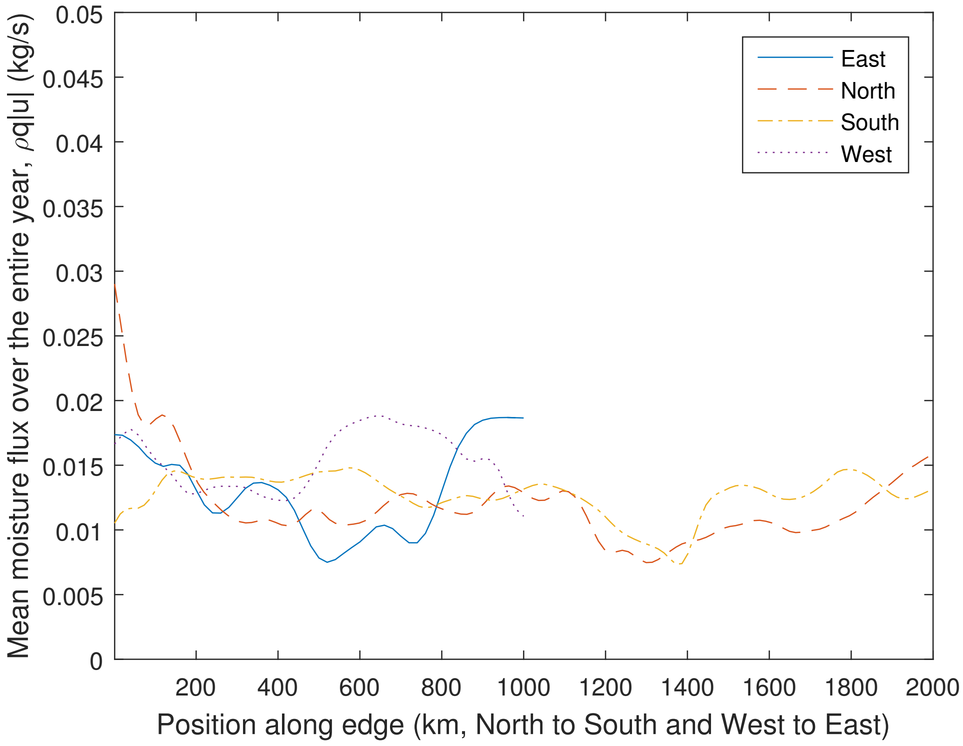

Fig. 15: Mean moisture flux over the entire year across each edge

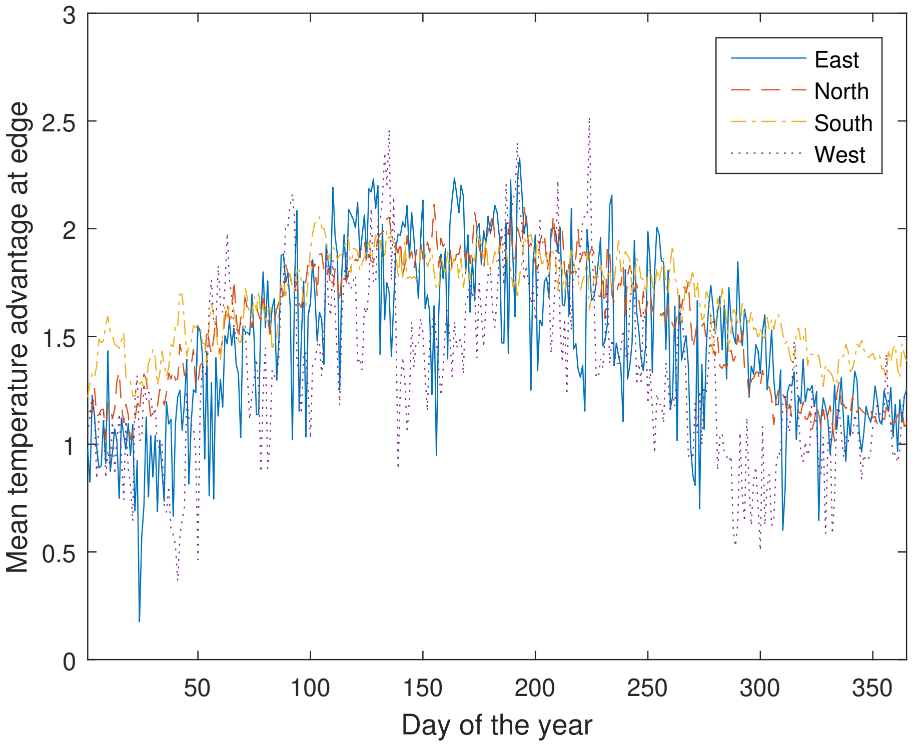

Fig. 16: Mean temperature advantage over the entire year across each edge

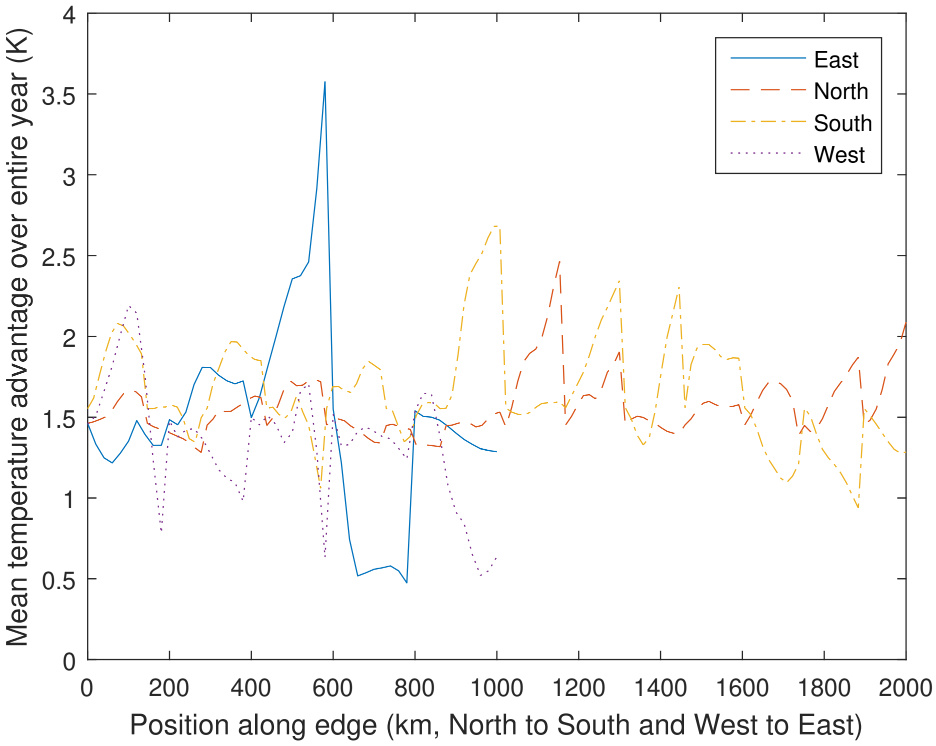

Fig. 17: Mean temperature advantage over the entire year across each edge

8.3 Other potential locations for deployment

In principle, the low-order model could be coupled with the CFS data for any region order to undertake the same analysis. By examining the parameters which drive the model, it may be possible to gain some insight into other potential locations for creating thermal mountains.

Clearly, solar insolation is a major contributor, therefore, proximity to the equator is one factor. Other factors include the albedo and the moisture flux. The albedo data used in this analysis covers the year 2005 and was sourced from ESA's GlobAlbedo project.[39] If the local albedo is higher, then the temperature contrast calculated by Equation 4 will be higher, enhancing the thermal mountain effect. The non-dimensionalised (all values divided through by the maximum albedo value) annual mean albedo is shown in Figure 18a. Of the regions closest to the equator, most of North Africa and the Arabian Peninsula have a higher albedo.

While thermal mountains have other applications, in the context of providing water to arid land, evaluating the annual albedo contrast is also relevant - if the albedo changes significantly, then vegetation is driving an annual change in albedo. If the albedo remains largely constant, then the region is either lifeless, or covered by vegetation without an annual albedo shift. Figure 18b shows the non-dimensionalised contrast in albedo between June and December. As this value approaches zero, this indicates an increasingly smaller annual albedo contrast, highlighting major desert and rainforest areas, along with permafrost. This criteria would seemingly advocate many regions, even discounting rainforest and permafrost areas. Notably, North Africa and the Arabian Peninsula are again amongst them, along with Australia, another location of multiple stable equilibrium discussed by Brovkin et al,[4] and also, a location proposed for irrigated afforestation by Ornstein et al.[5]

Lastly, the mean moisture flux is considered. Within Equation 8, precipitation output is linearly dependent upon both remaining driving factors of the model, humidity and wind speed. Therefore, moisture flux, the humidity multiplied by wind speed, can be taken as another metric. Figure 18c shows the nondimensionalised (again, all values divided through by the maximum moisture flux) mean moisture flux, based on the CFS dataset. While North Africa, the Arabian Peninsula and Australia are not amongst areas of high moisture flux, it can be seen that there is some level of moisture flux around their coasts.

These factors considered, North Africa, the Arabian Peninsula and Australia appear to be potential locations for thermal mountains.

9 CONCLUSIONS

This paper has presented a low-order engineering model of a thermal mountain system, covering thermodynamics, airflow and subsequent precipitation. The model has which has been used to provide approximate estimates of the scale of intervention necessary to irrigate a $1000\,\text{km} \times 2000\,\text{km}$ box of the Sahara. The scale of intervention has been determined to be extremely large, with a low-albedo surface area of $15\,600\,\text{km}^2$ at the lowest estimate. Agriculture and direct carbon capture have been investigated, along with sources of inaccuracy within the model. Potential improvements and refinements of the thermal mountain concept have also been discussed. While the scale of engineering intervention is clearly large, it is comparable in scale with other methods of sequestration, such as desalination-irrigation[5] or enhanced rock weathering.

CONFLICT OF INTEREST STATEMENT

There are no conflicts of interest to report.

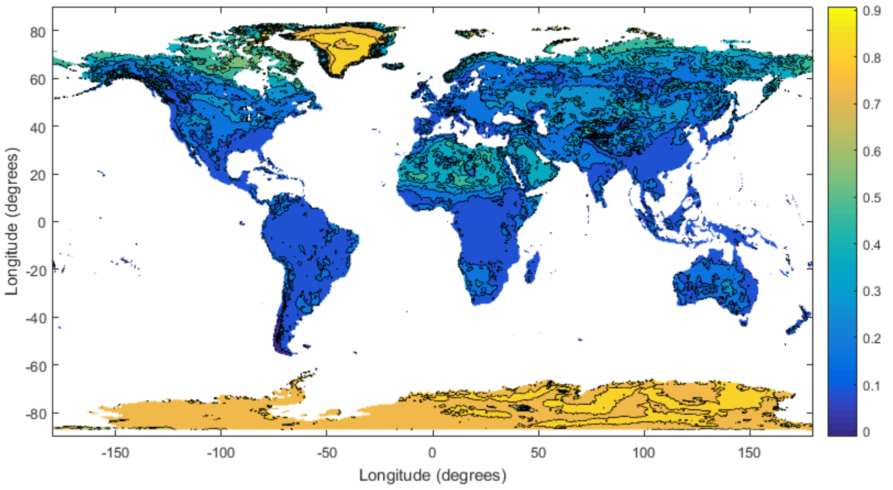

(a) Nondimensionaled mean albedo

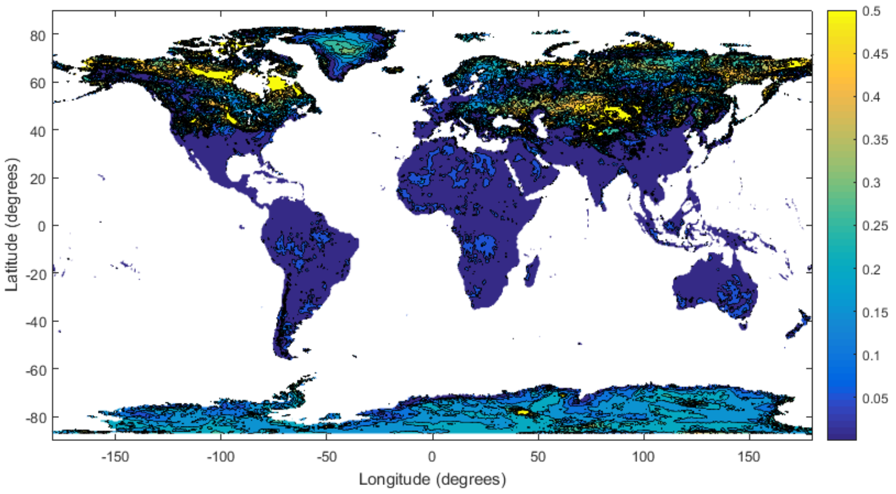

(b) Nondimensionaled albedo contrast from 1st of June to 1st of December

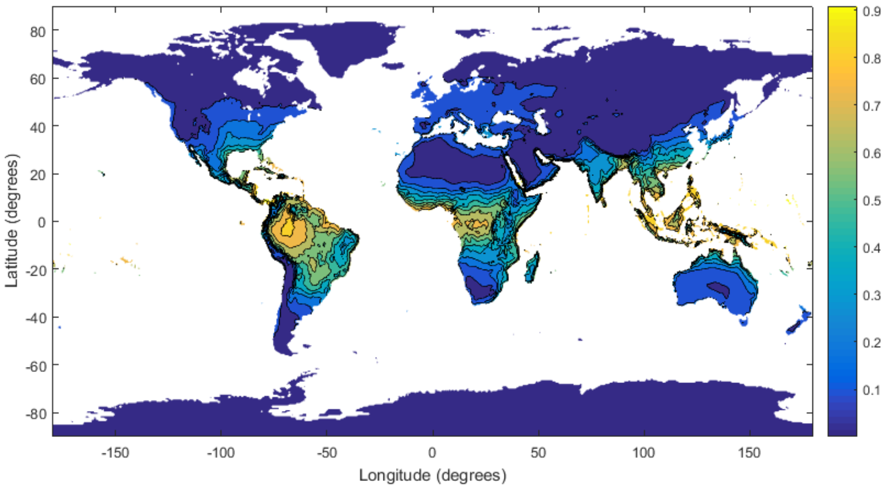

(c) Nondimensionaled mean annual moisture flux

Fig. 18: Albedo and moisture flux data across 2005

References

[1] D. A. Stainforth et al. “Uncertainty in predictions of the climate response to rising levels of greenhouse gases”. In: *Nature* 433 (Jan. 2005), pp. 403–406. URL: http://dx.doi.org/10.1038/nature03301.

[2] Kevin Anderson. “Duality in climate science”. In: *Nature Geoscience* 8 (Oct. 2015), pp. 898–900. URL: http://dx.doi.org/10.1038/ngeo2559.

[3] Rudolph Kuper and Stefan Kröpelin. “Climate-Controlled Holocene Occupation in the Sahara: Motor of Africa’s Evolution”. In: *Science* 313.5788 (2006), pp. 803–807. ISSN: 0036-8075. DOI: 10.1126/science.1130989. eprint: http://science.sciencemag.org/content/313/5788/803.full.pdf. URL: http://science.sciencemag.org/content/313/5788/803.

[4] Victor Brovkin et al. “On the stability of the atmosphere-vegetation system in the Sahara/Sahel region”. In: *Journal of Geophysical Research: Atmospheres* 103.D24 (Dec. 1998), pp. 31613–31624. ISSN: 0148-0227. DOI: 10.1029/1998JD200006. URL: https://doi.org/10.1029/1998JD200006.

[5] Leonard Ornstein, Igor Aleinov, and David Rind. “Irrigated afforestation of the Sahara and Australian Outback to end global warming”. In: *Climatic Change* 97.3 (Aug. 2009), pp. 409–437. ISSN: 1573-1480. DOI: 10.1007/s10584-009-9626-y. URL: https://doi.org/10.1007/s10584-009-9626-y.

[6] Tronje Peer Kemena et al. “Atmospheric feedbacks in North Africa from an irrigated, afforested Sahara”. In: *Climate Dynamics* (Sept. 2017). ISSN: 1432-0894. DOI: 10.1007/s00382-017-3890-8. URL: https://doi.org/10.1007/s00382-017-3890-8.

[7] James F. Black and Barry L. Tarmy. “The Use of Asphalt Coatings to Increase Rainfall”. In: *Journal of Applied Meteorology* 2.5 (Oct. 1963), pp. 557–564. ISSN: 0021-8952. DOI: 10.1175/1520-0450(1963)002⟨0557:TUOACT⟩2.0.CO;2. URL: https://doi.org/10.1175/1520-0450(1963)002%3C0557:TUOACT%3E2.0.CO;2.

[8] Nair Udaysankar S. et al. “The role of land use change on the development and evolution of the west coast trough, convective clouds, and precipitation in southwest Australia”. In: *Journal of Geophysical Research: Atmospheres* 116.D7 (Apr. 2011). ISSN: 0148-0227. DOI: 10.1029/2010JD014950. URL: https://doi.org/10.1029/2010JD014950.

[9] Wallace E Howell. “Comment on “The Use of Asphalt Coatings to Increase Rainfall””. In: *Journal of Applied Meteorology* 3.5 (1964), pp. 642–643.

[10] Tingzhen Ming, Wei Liu, Sylvain Caillol, et al. “Fighting global warming by climate engineering: Is the Earth radiation management and the solar radiation management any option for fighting climate change?” In: *Renewable and Sustainable Energy Reviews* 31 (2014), pp. 792–834.

[11] Lyla L Taylor et al. “Enhanced weathering strategies for stabilizing climate and averting ocean acidification”. In: *Nature Climate Change* 6.4 (2016), p. 402.

[12] Yan Li et al. “Climate model shows large-scale wind and solar farms in the Sahara increase rain and vegetation”. In: *Science* 361.6406 (2018), pp. 1019–1022.

[13] Marten Scheffer et al. “Synergy between small-and large-scale feedbacks of vegetation on the water cycle”. In: *Global change biology* 11.7 (2005), pp. 1003–1012.

[14] Suranjana Saha et al. “The NCEP Climate Forecast System Version 2”. In: *Journal of Climate* 27.6 (Sept. 2013), pp. 2185–2208. ISSN: 0894-8755. DOI: 10.1175/JCLI-D-12-00823.1. URL: https://doi.org/10.1175/JCLI-D-12-00823.1.

[15] NCAR. *The Climate Data Guide: Climate Forecast System Reanalysis (CFSR)*. https://climatedataguide.ucar.edu/climate-data/climate-forecast-system-reanalysis-cfsr. Last modified 05 Jul 2016. 2016.

[16] Zhihao Qin, Pedro Berliner, and Arnon Karnieli. “Micrometeorological modeling to understand the thermal anomaly in the sand dunes across the Israel–Egypt border”. In: *Journal of arid environments* 51.2 (2002), pp. 281–318.

[17] W CQJR Swinbank. “Long-wave radiation from clear skies”. In: *Quarterly Journal of the Royal Meteorological Society* 89.381 (1963), pp. 339–348.

[18] John A Duffie and William A Beckman. *Solar engineering of thermal processes*. John Wiley & Sons, 2013.

[19] Alain MB Passerat de Silans, Bruno A Monteny, and Jean Paul Lhomme. “Apparent soil thermal diffusivity, a case study: HAPEX-Sahel experiment”. In: *Agricultural and Forest Meteorology* 81.3-4 (1996), pp. 201–216.

[20] Engineering ToolBox. *Thermal Conductivity of common Materials and Gases. [online].* https://www.engineeringtoolbox.com/thermal-conductivity-d_429.html. Accessed on 2016-04-11. 2003.

[21] Hashem Akbari, Surabi Menon, and Arthur Rosenfeld. *Global cooling: effect of urban albedo on global temperature*. Tech. rep. Ernest Orlando Lawrence Berkeley NationalLaboratory, Berkeley, CA (US), 2007.

[22] Kenta Ogawa and Thomas Schmugge. "Mapping surface broadband emissivity of the Sahara Desert using ASTER and MODIS data". In: *Earth Interactions* 8.7 (2004), pp. 1–14.

[23] Robert Kenneth Wolfe and David C Colony. *Asphalt cooling rates: a computer simulation study*. Tech. rep. 1976.

[24] Joanne Starr Malkus and Melvin E Stern. "The flow of a stable atmosphere over a heated island, Part 1". In: *Journal of Meteorology* 10.1 (1953), pp. 30–41.

[25] V.P. Singh et al. *Encyclopedia of Snow, Ice and Glaciers*. Encyclopedia of Snow, Ice and Glaciers. Springer Netherlands, 2011. ISBN: 9789048126415. URL: https://books.google.co.uk/books?id=mKKtQR4T-1MC.

[26] US Geological Survey. "2013 Minerals Yearbook - China". In: (2013).

[27] Ronald B Smith and Idar Barstad. "A linear theory of orographic precipitation". In: *Journal of the Atmospheric Sciences* 61.12 (2004), pp. 1377–1391.

[28] AH El Nahry, RR Ali, and AA El Baroudy. "An approach for precision farming under pivot irrigation system using remote sensing and GIS techniques". In: *Agricultural Water Management* 98.4 (2011), pp. 517–531.

[29] P. Waller and M. Yitayew. *Irrigation and Drainage Engineering*. Springer International Publishing, 2014. ISBN: 9783319056982. URL: https://books.google.co.uk/books?id=MwasoAEACAAJ.

[30] M.H. Chaudhry. *Open-Channel Flow*. Springer US, 2007. ISBN: 9780387686486. URL: https://books.google.co.uk/books?id=-vqD7cYhX1oC.

[31] Harvey E Jobson. *Thermal modeling of flow in the San Diego Aqueduct, California, and its relation to evaporation*. 1122-1126. US Govt. Print. Off., 1980.

[32] Bradley A King and Dennis C Kincaid. “Optimal performance from center pivot sprinkler systems”. In: (1997).

[33] Florencia Montagnini and PKR Nair. “Carbon sequestration: an underexploited environmental benefit of agroforestry systems”. In: *New vistas in agroforestry*. Springer, 2004, pp. 281–295.

[34] Jose Luiz Stape, Dan Binkley, and Michael G Ryan. “Eucalyptus production and the supply, use and efficiency of use of water, light and nitrogen across a geographic gradient in Brazil”. In: *Forest Ecology and Management* 193.1-2 (2004), pp. 17–31.

[35] G Woldendorp, RJ Keenan, and MF Ryan. “Coarse woody debris in Australian forest ecosystems”. In: *A report for the national greenhouse strategy, Module* 6 (2002).

[36] Greet Janssens-Maenhout et al. “EDGAR v4. 3.2 Global Atlas of the three major Greenhouse Gas Emissions for the period 1970–2012”. In: *Earth Syst. Sci. Data Discuss* (2017). DOI: https://data.europa.eu/doi/10.2904/JRC_DATASET_EDGAR. URL: http://edgar.jrc.ec.europa.eu/overview.php?v=432&SECURE=123.

[37] H. Murakami. *Apparatus for producing a mass of water vapor, apparatus for producing, moving and climbing a mass of water vapor, and method of causing artificial stimulation of rain*. Patent number: US8439278B2. 2013.

[38] Jeffrey M Novak et al. “Impact of biochar amendment on fertility of a southeastern coastal plain soil”. In: *Soil science* 174.2 (2009), pp. 105–112.

[39] Jan-Peter Muller et al. “The ESA GlobAlbedo Project for mapping the Earth’s land surface albedo for 15 Years from European Sensors”. In: *Geophysical Research Abstracts*. Vol. 13. 2012, p. 10969.

APPENDIX

The results for the thermal mountain output when deployed along each edge can be modelled via a least-squares curve fit of the form $V = \alpha ln(L) + \beta$, where V is total yearly volumetric precipitation output and L is the length extending inwards from the edge of the box. If B is the breadth and L the length extending inwards from the edge of the box for a particular edge, then the area of the thermal mountain is simply:

$$A = BL \tag{A.1}$$

and by extension, the total area of thermal mountains deployed along two edges is:

$$A = A_1 + A_2 \tag{A.2}$$

Similarly, V_i ($i = 1, 2$) is the volumetric output of each edge, with its respective parameters from Table 2, such that:

$$V_i = \alpha_i ln(L_i) + \beta_i \tag{A.3}$$

and so, the combined volumetric precipitation output is:

$$V = V_1 + V_2 \tag{A.4}$$

which must equal the precipitation target, from Section 2. Equation A.3 can be rearranged as:

$$L_i = e^{\frac{V_i - \beta_i}{\alpha_i}} \tag{A.5}$$

Therefore, by combining Equations A.1, A.2 and A.5, Equation A.6 can be derived, which shows total area A to be defined as a function of dimension L_1:

$$A = B_1 L_1 + B_2 e^{\frac{V - \beta_1 - \beta_2}{\alpha_2}} L_1^{-\frac{\alpha_1}{\alpha_2}} \tag{A.6}$$

In order to minimise the required area for some total precipitation V, the turning point of A can be obtained:

$$\frac{dA}{dL_1} = \beta_1 + \beta_2 e^{\frac{V - \beta_1 - \beta_2}{\alpha_2}} - \frac{\alpha_1}{\alpha_2} L_1^{-\frac{\alpha_1}{\alpha_2} - 1} \tag{A.7}$$

It can be shown that the optimal value of L_1 is then obtained as:

$$L_1 = \left(\frac{B_2}{B_1} \frac{\alpha_1}{\alpha_2} e^{\frac{1 - \beta_1 - \beta_2}{\alpha_2}} \right)^{\frac{1}{\frac{\alpha_1}{\alpha_2} + 1}} \tag{A.8}$$

which minimises the total surface area for a given precipitation output. For the second length, the equation is the same but with the indices reversed. The parameters for each edge can be found in Table 2. Due to the diminishing returns with increasing *L*, it is more efficient in terms of total surface area to utilise two thermal mountains on different edges. Similar results can be derived for 3 or 4 edges, with further increasing efficiency. However, these approximations do not consider the possibility that the removal of moisture from the atmosphere at one edge may have a significant impact upon the available moisture at the others.